

A Quantum Instruction Set Implemented on a Superconducting Quantum Processor

M. Kjaergaard^{†,1,*} M. E. Schwartz^{2,†} A. Greene¹ G. O. Samach^{1,2} A. Bengtsson^{1,3}
 M. O’Keeffe² C. M. McNally¹ J. Braumüller¹ D. K. Kim² P. Krantz^{1,‡} M. Marvian^{1,4}
 A. Melville² B. M. Niedzielski² Y. Sung¹ R. Winik¹ J. Yoder² D. Rosenberg² K. Obenland²
 S. Lloyd^{1,4} T. P. Orlando¹ I. Marvian⁵ S. Gustavsson¹ and W. D. Oliver^{1,2,6,7}

¹*Research Laboratory of Electronics, Massachusetts Institute of Technology, Cambridge, MA 02139, USA*

²*MIT Lincoln Laboratory, Lexington, MA 02421, USA*

³*Microtechnology and Nanoscience, Chalmers University of Technology, Göteborg, SE-412 96, Sweden*

⁴*Department of Mechanical Engineering, Massachusetts Institute of Technology, Cambridge, MA 02139, USA*

⁵*Departments of Physics & Electrical and Computer Engineering, Duke University, Durham, NC 27708, USA*

⁶*Department of Physics, Massachusetts Institute of Technology, Cambridge, MA 02139, USA*

⁷*Department of Electrical Engineering & Computer Science,
 Massachusetts Institute of Technology, Cambridge, MA 02139, USA*

(Dated: July 28, 2022)

A quantum algorithm consists of a sequence of operations and measurements applied to a quantum processor. To date, the instruction set which defines this sequence has been provided by a classical computer and passed via control hardware to the quantum processor. Here, we demonstrate the first experimental realization of a quantum instruction set, in which a fixed sequence of classically-defined gates perform an operation that is fully determined only by a quantum input to the fixed sequence. Specifically, we implement the density matrix exponentiation algorithm, which consumes N copies of the instruction state ρ to approximate the operation $e^{-i\rho\theta}$ (θ an arbitrary angle). Our implementation relies on a 99.7% fidelity controlled-phase gate between two superconducting transmon qubits. We achieve an average algorithmic fidelity ≈ 0.9 , independent of the setting of ρ , to circuit depth nearly 90. This new paradigm for quantum instructions has applications to resource-efficient protocols for validating entanglement spectra, principal component analysis of large quantum states, and universal quantum emulation.

INTRODUCTION

Programmable computation, whether classical or quantum, consists of two fundamental components: an instruction set, and a machine to execute those instructions. For classical computation, there is no intrinsic distinction between these components—the same physical instrument may be used both to generate and execute the instructions (Figure 1A) [1]. To date, the same has not been true for experimental demonstrations of quantum computing, whether in gate-based systems [2], quantum annealing [3], or one-way quantum computing [4]. In conventional quantum computing applications, shown schematically in Figure 1B, the instructions are programmed using classical resources [5] and then delivered via hardware to a quantum processor that executes the instructions [6–8]. In other words, the parity between instruction set and the processor executing the instructions is broken: one is fully classical, the other quantum.

Here, we demonstrate an implementation of *quantum* instructions, in which a quantum state provides on-the-fly programming to a quantum computer (Figure 1C). In this approach, a fixed sequence of classically-defined gates forms the scaffolding for a variable operation on a target system σ ; an auxiliary quantum state with density matrix ρ completes the encoding of the instructions. This hybrid approach to quantum programming partially restores the parity between the instructions and the pro-

cessor in a quantum computer.

Quantum instructions have a variety of applications, including executing private quantum functions [9] and quantum simulation [10]. Quantum instructions are central to an efficient implementation of quantum emulation [9], which enables the implementation of an unknown unitary U with a finite set of known input-output relations $\{\rho_{\text{in}}\} \xrightarrow{U} \{\rho_{\text{out}}\}$. Quantum emulation consumes fewer copies of the instruction qubits than would be sufficient for tomographic reconstruction, enabling the application of U to an arbitrary state without compromising the privacy of U itself. A quantum instruction set has also been theoretically proven to provide quantum speedups in quantum semi-definite programming [11]. Additionally, if a Hamiltonian is encoded in the instruction state, quantum instructions enable sample-optimal Hamiltonian simulation [10].

A quantum instruction set can be implemented efficiently using an approach called density matrix exponentiation (DME) [12]. DME consumes N copies of the quantum instruction density matrix ρ , and approximately performs the unitary gate $e^{-i\rho\theta}$, where θ is an arbitrary angle. It has been shown that DME asymptotically outperforms any tomographic strategy to implement $e^{-i\rho\theta}$ [10, 12]. Without access to a quantum instruction set, implementing $e^{-i\rho\theta}$ necessitates a full tomographic construction of ρ . This in turn requires $\mathcal{O}(d^2/\epsilon^2)$ copies of ρ , where d is the dimension of the in-

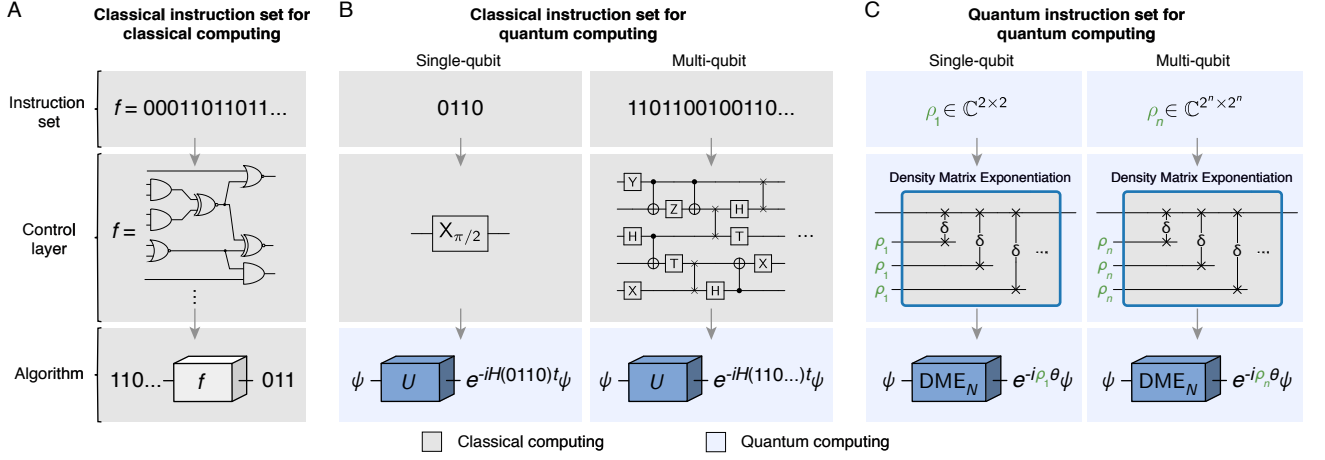


FIG. 1. (A) Schematic representation of classical computing. Instructions are expressed by a classical function f defined by a bitstring ‘00011...’, and is then executed on a dataset 110.... (B) Schematic representation of conventional quantum computing. The instruction set encoding a quantum circuit is generated using classical resources. A control layer generates the corresponding gate sequence, which is sent to the quantum hardware and implements the operation $U = \exp(-iH(0110)t)$. Here $H(0110)$ is the Hamiltonian with parameters given by the bitstring 0110. (C) Quantum instruction set using the density matrix exponentiation (DME) algorithm. A single-qubit instruction (ρ_1) is used to implement the operator $DME_N(\rho_1, N, \theta) \approx e^{-i\rho_1\theta}$ using a sequence of N partial SWAP operations, each supplied with a new copy of ρ_1 . A multi-qubit program using quantum instructions shares the same structure of the classical gates.

struction system and ϵ is the desired precision [13]. DME as implemented with quantum instructions requires only $\mathcal{O}(\theta^2/\epsilon)$ copies, resulting in an exponential reduction in resource requirements [12]. This advantage makes DME a powerful platform to implement quantum operations based on quantum states, avoiding the need for classical learning of ρ .

In addition to implementing quantum instructions, DME is a useful tool for using the target system to learn about the instruction set. In particular, a controlled-DME protocol combined with quantum phase estimation can be used to extract the dominant eigenvalues and eigenvectors of ρ , using only $\mathcal{O}(\theta^2/\epsilon)$ copies [10, 12]. Furthermore, if ρ is a large entangled state, DME efficiently reveals its entanglement spectrum without full tomography [14]. Thus, quantum instructions provide a powerful toolset for efficient quantum computation (using ρ to manipulate σ) and quantum metrology (using σ to study ρ).

ALGORITHM IMPLEMENTATION

A practical protocol for implementing DME, first proposed in Ref. [12], utilizes partial SWAP interactions between a target state σ and N copies of the instruction state ρ . We will denote this protocol DME_N . The SWAP matrix exchanges the state of two qubits according to $\text{SWAP}(\sigma \otimes \rho) = \rho \otimes \sigma$. The DME_N algorithm relies on the observation that:

$$\begin{aligned} \text{Tr}_\rho [e^{-i\text{SWAP}\delta} \sigma \otimes \rho e^{i\text{SWAP}\delta}] &= \sigma - i\delta[\rho, \sigma] + \mathcal{O}(\delta^2) \\ &= e^{-i\rho\delta} \sigma e^{i\rho\delta} + \mathcal{O}(\delta^2). \end{aligned} \quad (1)$$

That is, after a partial SWAP, defined as $\delta\text{SWAP} \equiv e^{-i\text{SWAP}\delta}$ [15], σ undergoes unitary evolution of the form $e^{-i\rho\delta}$ (up to first order in δ). Applying this technique serially (Figure 1C) by introducing a new copy of ρ for each of N δSWAP operations with $\delta = \theta/N$ implements the operator

$$DME_N(\rho, N, \theta) \rightarrow e^{-i\rho\theta} + \mathcal{O}\left(\frac{\theta^2}{N}\right). \quad (2)$$

For intuition, if ρ is a single-qubit pure state, DME_N rotates σ about the axis defined by the Bloch sphere vector of ρ , through an angle θ . The physics of DME_N are related to the Trotterization of non-commuting Hamiltonians to perform quantum simulation [16]. Dividing a quantum simulation into smaller steps reduces errors stemming from the Trotter approximation, and similarly, supplying DME_N with more copies reduces algorithmic error.

In Figure 2, we implement a variant of DME_N in which one qubit serves as the target upon which the algorithm acts, and the other provides all N copies of the quantum instruction. This resource-efficient protocol, which we denote DME , trades a moderate increase in algorithmic error for a significant reduction in the required number of qubits. Our approach relies on approximately re-initializing the instruction qubit after each δSWAP , without the need for active feedback, using a novel probabilistic operation which we call the *simulated quantum measurement* (SQM) [17].

For small δ , the state of the target and instruction qubits are nearly unaffected after a δSWAP . In this case, a measurement of ρ in its eigenbasis approximately ‘resets’ the qubit by projecting it onto its quantization axis.

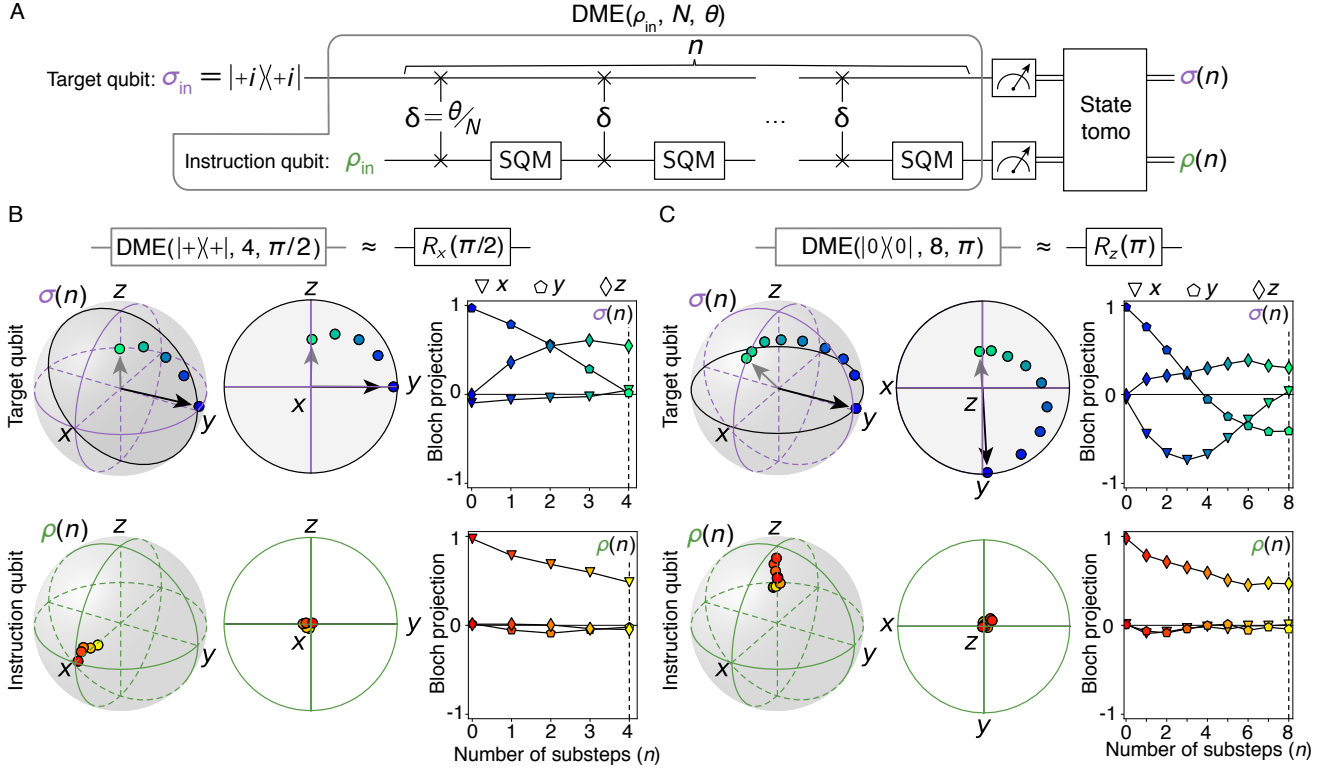


FIG. 2. (A) Two-qubit DME implementation using the SQM gate to approximately reinitialize the instruction qubit to ρ_{in} . The substep parameter n is stepped from 0 to N . We perform n rounds of δ SWAP + SQM, measure the two-qubit density matrix, and trace over each subsystem to extract the individual density matrices $\sigma(n)$ and $\rho(n)$. (B) Substeps of $\text{DME}(|+\rangle\langle+|, 4, \pi/2)$, corresponding to $R_x(\pi/2)$ on the target qubit at the final step ($n = N$). Black lines are guides to the eye. (C) Substeps of $\text{DME}(|0\rangle\langle 0|, 8, \pi)$, corresponding to $R_z(\pi)$ on the target qubit at $n = N$.

SQM mimics this effect without actually performing a measurement by constructing a dephasing channel corresponding to the axis of ρ .

The SQM operation randomly applies either an identity gate ($\mathbb{1}$) or a π -rotation in the instruction qubit eigenbasis:

$$\boxed{\text{SQM}_\nu} = \begin{cases} \mathbb{1} & \text{with } p = 0.5 \\ R_\nu(\pi) & \text{with } p = 0.5 \end{cases} \quad (3)$$

where ν is a normalized vector with x -, y -, z - components parallel to the instruction state. We focus on instruction states representing the cardinal points of the Bloch sphere, namely the z -polarized states $|0\rangle\langle 0|$, $|1\rangle\langle 1|$, the x -polarized states $|\pm\rangle\langle\pm|$, and the y -polarized states $|\pm i\rangle\langle\pm i|$. In these cases, SQM represents a probabilistic application of a Pauli gate. When averaged over many randomizations, SQM is identical to a measurement whose outcomes are ignored, while only requiring the time span of a single-qubit gate. We incorporate SQM into our circuit (Figure 2A) by interleaving δ SWAP operations with SQM on the instruction qubit, executing many instantiations of the circuit with random choices of $\{\mathbb{1}, R_\nu(\pi)\}$ for each SQM and each instantiation, and averaging together the outcomes [18].

Because the SQM-enabled reset of ρ is approximate, its use introduces additional error, on the same order of magnitude as the algorithmic error in DME_N [18]. The two-qubit implementation of DME has the following error budget:

$$\text{DME}(\rho, N, \theta) \rightarrow e^{-i\rho\theta} + \underbrace{\mathcal{O}(\frac{\theta^2}{N})}_{\text{Finite } N} + \underbrace{\mathcal{O}(\frac{\theta^2}{N})}_{\text{SQM}}. \quad (4)$$

Our experiment utilizes two frequency-tunable superconducting ‘asymmetric’ transmon qubits [19, 20] in an ‘xmon’ layout [18, 21]. The native gate set comprises microwave-driven single-qubit x - and y - rotations $R_X(\phi)$ and $R_Y(\phi)$, single-qubit virtual- z rotations $R_Z(\phi)$, and the two-qubit controlled-phase (CZ) gate [22]. We implement the δ SWAP using single-qubit gates and the entangling CZ gate. δ SWAP has an optimal decomposition [23]

$$\delta\text{SWAP} = \begin{array}{c} \boxed{} \text{---} \bullet \text{---} \boxed{} \text{---} \bullet \text{---} \boxed{} \text{---} \bullet \text{---} \boxed{} \\ \boxed{} \text{---} \bullet \text{---} \boxed{} \text{---} \bullet \text{---} \boxed{} \text{---} \bullet \text{---} \boxed{} \end{array} := \frac{\pi}{\delta} \quad (5)$$

where each $\boxed{}$ represents a general single-qubit gate that depends on the value of δ and \bullet is the CZ gate. The open-source software package Cirq [24] is used to determine the appropriate single-qubit gate parameters for a

given δSWAP [18]. Our δSWAP construction allows us to rely solely on high-fidelity gates whose performance can be validated and efficiently optimized. In particular, we calibrate a numerically optimized 99.7% fidelity CZ gate [25, 26], using a symmetrized optimal control waveform that reduces leakage and noise-sensitivity [18, 27–29].

In Figure 2B-C, we validate the concept of the quantum instruction set and visualize substeps of a DME implementation. We choose a fixed target state $\sigma_{\text{in}} = |+\rangle\langle+|$ and vary both the instruction state ρ_{in} and total phase θ . We interrupt the algorithm after n substeps of $\delta\text{SWAP} + \text{SQM}$ and perform state tomography, averaging together all SQM randomizations to produce a single density matrix [18, 30]. Figure 2B shows an implementation of $\text{DME}(|+\rangle\langle+|, 4, \pi/2)$. Since the instruction is x -polarized, this operation performs $R_X(\pi/2)$ on σ_{in} (up to algorithmic errors). Figure 2C shows DME with new parameters, namely $\text{DME}(|0\rangle\langle 0|, 8, \pi)$, corresponding to an implementation of $R_Z(\pi)$. In both cases, $\sigma(n)$ undergoes partial rotation at each step about an axis defined by ρ_{in} ; $\rho(n)$ maintains its initial direction but undergoes depolarization. Though the classical instructions are identical in these two cases (modulo the SQM randomizations), the change in the quantum instructions causes the DME algorithm to perform a different operation on σ . This demonstrates and validates the fundamental underlying principle of DME and of using quantum states as instruction sets for programming operations on other quantum states.

ALGORITHM CHARACTERIZATION

We now assess DME in the context of an imperfect processor with noise-induced errors in addition to algorithmic errors (Figure 3). Here, we fix target $\sigma_{\text{in}} = |0\rangle\langle 0|$ and instruction $\rho_{\text{in}} = |+\rangle\langle+|$, and vary total steps N . This allows us to probe the interplay between algorithmic error (which decreases with N) and noise-induced errors (which increases with N). We use two angles, $\theta = \pi$ and $\theta = \pi/2$, to elucidate the effects of changing the overall angle.

For each experiment, we perform the full algorithm $\text{DME}(\rho_{\text{in}}, N, \theta)$ (randomizing over SQM instances), tomographically reconstruct the joint state, and trace over the instruction qubit to extract the final target density matrix $\sigma(N)$. We then calculate the fidelity to the output of an idealized DME given by $\sigma_{\text{ideal}} = e^{-i\rho_{\text{in}}\theta}\sigma_{\text{in}}e^{i\rho_{\text{in}}\theta}$; that is, a perfect rotation with no algorithmic error. We define fidelity according to Ref. [31]

$$F_s(\sigma, \sigma') = \text{Tr} \left(\sqrt{\sqrt{\sigma'}\sigma\sqrt{\sigma'}} \right)^2. \quad (6)$$

To extract error bars we perform bootstrap sampling for each N and θ [18, 32].

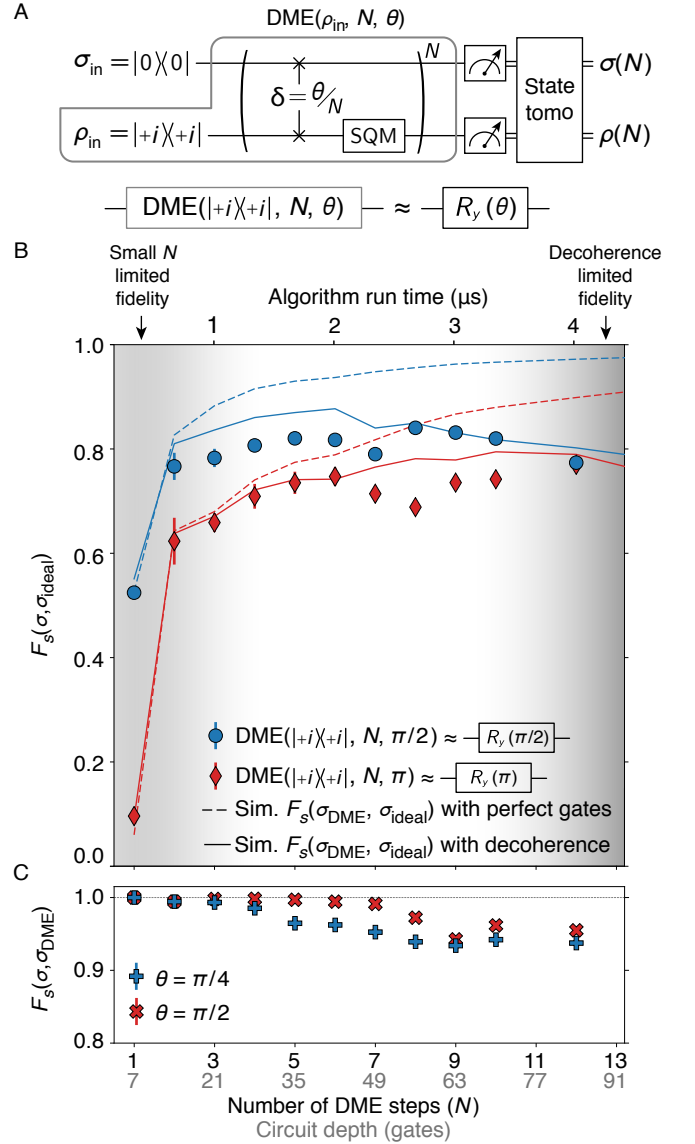


FIG. 3. (A) Circuit schematic for $\text{DME}(\rho_{\text{in}} = |+\rangle\langle+|, N, \theta)$. Target qubit is initialized in $\sigma_{\text{in}} = |0\rangle\langle 0|$. (B) Fidelity of the final target qubit state, $\sigma(N)$, to the ideal state $\sigma_{\text{ideal}} = e^{-i\rho_{\text{in}}\theta}\sigma_{\text{in}}e^{i\rho_{\text{in}}\theta}$. The x -axis shows the number of Trotter steps N (bottom, black), circuit depth (bottom, gray), and active circuit clock time (top). Data for $\theta = \pi$ ($\pi/2$) are shown with red/ \diamond (blue/ \circ) markers. Dashed lines of the respective colors indicate the algorithmic error assuming perfect gates; solid lines represent the simulated DME performance in the presence of amplitude damping and depolarizing channels. (C) Fidelity of $\sigma(N)$ to simulated DME performance with ideal gates (denoted σ_{DME}).

There are two sources of error we must consider in understanding the output of the DME protocol: the approximate nature of the algorithm and imperfections in the quantum processor. To understand the algorithmic error, we calculate σ_{DME} , the outcome of a simulation of the DME circuit (including algorithmic error) with perfect gates. We sample every possible combination of SQM gates for a DME circuit of length N and simu-

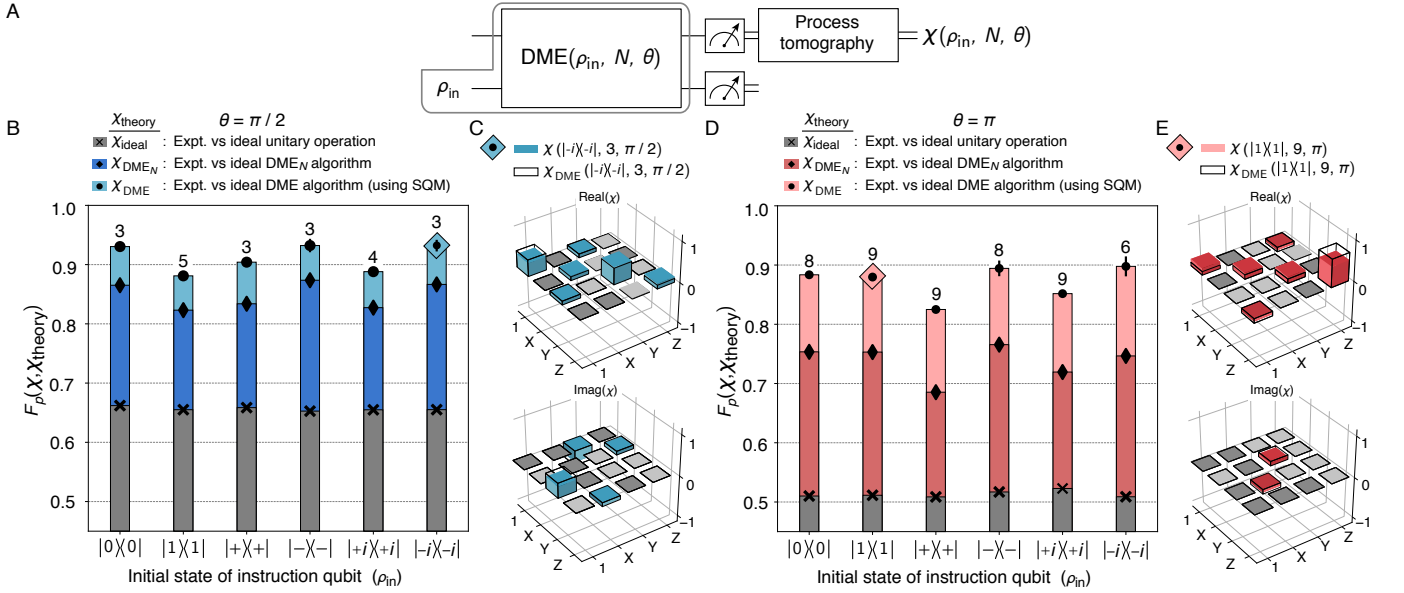


FIG. 4. (A) Circuit schematic. Single-qubit process tomography is performed for a set of six instruction states ρ_{in} representing cardinal points of the Bloch sphere. (B, D) Process fidelities with $\theta = \pi/2$ (B) and $\theta = \pi$ (D). Grey (\times marker) denotes the fidelity to the ideal process χ_{ideal} . The data are presented at $N = N_{\text{opt}}$, where the fidelity to χ_{ideal} is maximized; N_{opt} is indicated by the number above each bar. Dark blue/red (\diamond marker) indicates fidelity to a theoretical DME_N process (denoted χ_{DME_N}), evaluated at $N = N_{\text{opt}}$. Light blue/red (\circ marker) shows the fidelity to the as-implemented DME protocol using SQM (denoted χ_{DME}). The process map for the point enclosed by a blue [red] diamond is shown in (C) [(E)]. Colored process matrix elements indicate points with magnitude $\chi_{ij} > 0.02$; other elements are grey for clarity of scale. Black wire frames denote the expected process χ_{DME} .

late the application of each circuit to the experimentally-measured $\rho_{\text{in}} \otimes \sigma_{\text{in}}$ (thus accounting for state-preparation errors). We average all simulated outcomes and trace over the instruction qubit to generate σ_{DME} . The fidelity $F_s(\sigma_{\text{DME}}, \sigma_{\text{ideal}})$ indicates the error due solely to the approximate nature of DME (Figure 3B, dashed lines). Figure 3C shows the fidelity of the measured state $\sigma(N)$ to the ideal algorithm performance, $F_s(\sigma(N), \sigma_{\text{DME}})$. To circuit depth approaching 90, this fidelity exceeds 0.90.

We next account for the effects of imperfections in the physical processor by building a model of DME performance in the presence of processor noise. To the DME circuit with perfect gates we add amplitude-damping and dephasing channels with coherence parameters consistent with independent measurements [18]. The fidelity between the model including decoherence effects and σ_{ideal} is plotted in Figure 3B (solid lines), and shows good agreement with experimental data, indicating we are mostly limited by decoherence effects, and not coherent errors in the gates.

Both the simulated and experimental curves reveal an interplay between finite N error and processor error. At small N , the error is dominated by the approximate nature of DME as given in Eq. (4). The error is greater for larger θ , consistent with error scaling as $\mathcal{O}(\theta^2/N)$. For large N , the algorithmic error improves and the processor's performance is instead limited by finite gate fidelity; here, the curves for $\theta = \pi$ and $\theta = \pi/2$ begin to converge. The algorithm is at its most accurate for intermediate N ,

where algorithmic error is relatively low and the circuit is sufficiently free of compounding physical errors. This tradeoff (improved performance with increasing circuit depth, until gate fidelities become limiting) is a generic property of Trotterized quantum algorithms on noisy processors in the absence of error-correction protocols [33].

In Figure 4, we perform process tomography to fully characterize the quantum channel implemented by DME. We employ standard process tomography techniques [18] to reconstruct $\text{DME}(\rho_{\text{in}}, N, \theta)$ for a set of ρ_{in} comprising the six cardinal points of the Bloch sphere. We project the measured process onto the space of completely positive, trace-preserving process maps, with a χ -matrix representation in the Pauli basis denoted $\chi(\rho_{\text{in}}, N, \theta)$ [34]. For each ρ_{in} , we sweep N to find the optimal point N_{opt} , defined as that which has the highest process fidelity to the pure rotation $U_{\text{ideal}} = e^{-i\rho_{\text{in}}\theta}$. The process fidelity between two χ -matrices is defined as $F_p(\chi, \chi') = \text{Tr}(\sqrt{\sqrt{\chi'}\chi\sqrt{\chi'}})^2$ [35]. The mean N_{opt} for $\theta = \pi/2$ is 4, at circuit depth 28; for $\theta = \pi$ this increases to 8, at circuit depth 56.

In Figure 4B-C we plot the process fidelity at N_{opt} to several theoretical processes, elucidating the error budget in DME. The fidelity to χ_{ideal} , corresponding to the perfect rotation U_{ideal} , is plotted in grey. $F_p(\chi, \chi_{\text{ideal}})$ is greater for $\theta = \pi/2$ than for $\theta = \pi$, as expected from the $\mathcal{O}(\theta^2/N)$ scaling of the algorithmic error, and is consistent for all cardinal settings of the instruction state.

The fidelity $F_p(\chi, \chi_{\text{ideal}})$ reflects the error arising from the Trotterized nature of DME, combined with the errors from imperfect gates and the approximate nature of SQM.

We next compare our SQM-enabled algorithm to the original DME_N proposal requiring N copies of ρ_{in} . We label this theoretical process χ_{DME_N} and calculate the fidelity $F_p(\chi, \chi_{\text{DME}_N})$, shown in dark blue/red. This fidelity combines the physical errors arising from our imperfect gates and the error from not using N fresh copies of ρ_{in} . The difference between $F_p(\chi, \chi_{\text{DME}_N})$ and $F_p(\chi, \chi_{\text{ideal}})$ is a reflection of finite N error.

Finally, we plot the fidelity between our measured process and χ_{DME} , a simulated version of the resource-efficient DME algorithm, shown in light blue/red. This fidelity compares the experimental implementation of DME to a simulation using perfect operations, and is therefore the most direct metric for the performance of our processor. The theoretical χ_{DME} is calculated by sampling all SQM randomizations and averaging their effect. The average process fidelity $F_p(\chi, \chi_{\text{DME}})$ over all instruction settings is 0.91 for $\theta = \pi/2$ and 0.87 for $\theta = \pi$; this algorithmic fidelity is overall reduced for $\theta = \pi$ because N_{opt} occurs at deeper circuit depth.

CONCLUSION

We have demonstrated the first experimental implementation of a quantum program whose instructions are stored in a quantum state. Our implementation relies on a 99.7% fidelity CZ gate combined with a novel simulated quantum measurement technique, to implement a proof-of-principle version of the density matrix exponentiation algorithm, achieving fidelities close to 0.9 out to circuit depth of nearly 90 sequential gates. While we use pure states to form the quantum instruction set, the DME algorithm generalizes to mixed states and efficiently extends to multi-qubit systems, requiring only the ability to perform controlled versions of the SWAP operation between pairs of target and instruction qubits [9, 10, 14, 36]. This scaling makes DME an attractive option for guaranteed private quantum software [9], certain tomographic applications [12], efficient sensing of entanglement spectra of large states [14], and for quantum machine learning techniques on quantum data [37].

Funding: MK gratefully acknowledges support from the Carlsberg Foundation during part of this work. AG acknowledges funding from the 2019 Google US/Canada PhD Fellowship in Quantum Computing. IM acknowledges funding from NSF grant FET-1910859. This research was funded in part by the U.S. Army Research Office Grant W911NF-18-1-0411 and the Assistant Secretary of Defense for Research & Engineering under

Air Force Contract No. FA8721-05-C-0002. Opinions, interpretations, conclusions, and recommendations are those of the authors and are not necessarily endorsed by the United States Government.

Author contributions: MK, MS, AG, GS, AB, CM, and PK performed the experiments. MK, MS, AG, GS, MO, CM, and KO developed analytical tools and analyzed data. MK, MS, AG, AB, JB, RW, YS, and SG developed experimental control tools. MK, MO, CM, and KO performed algorithm simulations under realistic noise models. MK, MS, AG, GS, MO, MM, DR, SL, and IM developed the resource-efficient DME protocol. DK, AM, BN, and JY fabricated devices. TO, SG, and WO provided experimental oversight and support. All authors contributed to the discussion of the results and the manuscript.

Acknowledgements: The authors gratefully acknowledge feedback on the manuscript from Antti Vepsäläinen, Cyrus Hirjibehedin, Kyle Serniak, Thomas Hazard, and Steven Weber.

Competing interests: The authors declare no competing interests.

* mortenk@mit.edu

† Authors contributed equally to this work

‡ Current address: Microtechnology and Nanoscience, Chalmers University of Technology

- [1] A. M. Turing, *Proc. London Math. Soc.* **s2-42**, 230 (1937).
- [2] D. P. DiVincenzo, *Proc. R. Soc. London A* **454**, 261 (1998).
- [3] E. Farhi, J. Goldstone, S. Gutmann, M. Sipser, *arXiv:quant-ph/0001106* (2000).
- [4] R. Raussendorf, H. J. Briegel, *Phys. Rev. Lett.* **86**, 5188 (2001).
- [5] R. S. Smith, M. J. Curtis, W. J. Zeng, *arXiv:1608.03355* (2016).
- [6] F. Arute, *et al.*, *Nature* **574**, 505 (2019).
- [7] R. Harris, *et al.*, *Science* **361**, 162 (2018).
- [8] S. Barz, *et al.*, *Science* **335**, 303 (2012).
- [9] I. Marvian, S. Lloyd, *arXiv:1606.02734* (2016).
- [10] S. Kimmel, C. Y.-Y. Lin, G. H. Low, M. Ozols, T. J. Yoder, *npj Quantum Inf* **3**, 1 (2017).
- [11] F. G. S. L. Brando, *et al.*, *arXiv:1710.02581* (2019).
- [12] S. Lloyd, M. Mohseni, P. Rebentrost, *Nat. Phys.* **10**, 631 (2014).
- [13] J. Haah, A. W. Harrow, Z. Ji, X. Wu, N. Yu, *IEEE Transactions on Information Theory* **63**, 5628 (2017).
- [14] H. Pichler, G. Zhu, A. Seif, P. Zoller, M. Hafezi, *Phys. Rev. X* **6**, 041033 (2016).
- [15] Y. Salathé, *et al.*, *Phys. Rev. X* **5**, 021027 (2015).
- [16] S. Lloyd, *Science* **273**, 1073 (1996).
- [17] A. Greene, *et al.*, *in preparation* (2020).
- [18] See Supplemental Material for more information.

- [19] J. Koch, *et al.*, *Phys. Rev. A* **76**, 042319 (2007).
- [20] M. D. Hutchings, *et al.*, *Phys. Rev. App.* **8**, 044003 (2017).
- [21] R. Barends, *et al.*, *Phys. Rev. Lett.* **111**, 080502 (2013).
- [22] P. Krantz, *et al.*, *App. Phys. Rev.* **6**, 021318 (2019).
- [23] F. Vatan, C. Williams, *Phys. Rev. A* **69**, 032315 (2004).
- [24] Cirq-v0.5.0, <https://github.com/quantumlib/cirq>.
- [25] J. Kelly, *et al.*, *Phys. Rev. Lett.* **112** (2014).
- [26] F. W. Strauch, *et al.*, *Phys. Rev. Lett.* **91**, 167005 (2003).
- [27] M. Rol, *et al.*, *Phys. Rev. Lett.* **123**, 120502 (2019).
- [28] J. M. Martinis, M. R. Geller, *Phys. Rev. A* **90**, 022307 (2014).
- [29] W. D. Oliver, *et al.*, *Science* **310**, 1653 (2005).
- [30] D. F. V. James, P. G. Kwiat, W. J. Munro, A. G. White, *Phys. Rev. A* **64**, 052312 (2001).
- [31] M. M. Wilde, *Quantum Information Theory 2nd ed.* (Cambridge University Press, 2017).
- [32] B. Efron, *Ann. Statist.* **7**, 1 (1979).
- [33] R. Rines, K. Obenland, I. Chuang, *arXiv:1905.10724* (2019).
- [34] G. C. Knee, E. Bolduc, J. Leach, E. M. Gauger, *Phys. Rev. A* **98**, 062336 (2018).
- [35] M. A. Nielsen, *Phys. Lett. A* **303**, 249 (2002).
- [36] Y. Y. Gao, *et al.*, *Nature* **566**, 509 (2019).
- [37] J. Biamonte, *et al.*, *Nature* **549**, 195 (2017).

Supplementary material for “A Quantum Instruction Set Implemented on a Superconducting Quantum Processor”

M. Kjaergaard^{†,1,*} M. E. Schwartz^{2,†} A. Greene¹ G. O. Samach^{1,2} A. Bengtsson^{1,3}
M. O’Keeffe² C. M. McNally¹ J. Braumüller¹ D. K. Kim² P. Krantz^{1,‡} M. Marvian^{1,4}
A. Melville² B. M. Niedzielski² Y. Sung¹ R. Winik¹ J. Yoder² D. Rosenberg² K. Obenland²
S. Lloyd^{1,4} T. P. Orlando¹ I. Marvian⁵ S. Gustavsson¹ and W. D. Oliver^{1,2,6,7}

¹*Research Laboratory of Electronics, Massachusetts Institute of Technology, Cambridge, USA, MA 02139*

²*MIT Lincoln Laboratory, 244 Wood Street, Lexington, USA, MA 02421*

³*Microtechnology and Nanoscience, Chalmers University of Technology, Göteborg, Sweden, SE-412 96*

⁴*Department of Mechanical Engineering, Massachusetts Institute of Technology, Cambridge, Massachusetts 02139, USA*

⁵*Departments of Physics & Electrical and Computer Engineering, Duke University, Durham, North Carolina 27708, USA*

⁶*Department of Physics, Massachusetts Institute of Technology, Cambridge, USA, MA 02139*

⁷*Department of Electrical Engineering & Computer Science,
Massachusetts Institute of Technology, Cambridge, USA, MA 02139*

(Dated: July 28, 2022)

CONTENTS

A. Parameters of the device	1
B. Algorithmic error in DME_N	3
C. Algorithmic error due to SQM	5
D. Details of the compilation	6
E. Benchmarking qubit operations	8
1. Single qubit gates: Randomized benchmarking	8
2. Two qubit gates: Randomized benchmarking	9
3. Two qubit gates: Reducing small coherent errors	10
F. Details of state and process tomography	11
G. Details of bootstrap error analysis	12
H. Quantifying the impacts of finite SQM randomizations	13
I. Circuit simulation with noise	14
References	15

Appendix A: Parameters of the device

The quantum processor used in this work has three asymmetric ‘xmon’-style qubits in a linear chain [S1–S3]. We use the two leftmost qubits in this protocol; the third is detuned and idles in its ground state. Figure S1(a) shows a schematic of the readout- and control- setup used to control the qubits. Figure S1(b) shows a scanning electron micrograph of a device identical to the one used in this work. In Table S1 we summarize the parameters of the two

* mortenk@mit.edu

† Authors contributed equally to this work

‡ Current address: Microtechnology and Nanoscience, Chalmers University of Technology

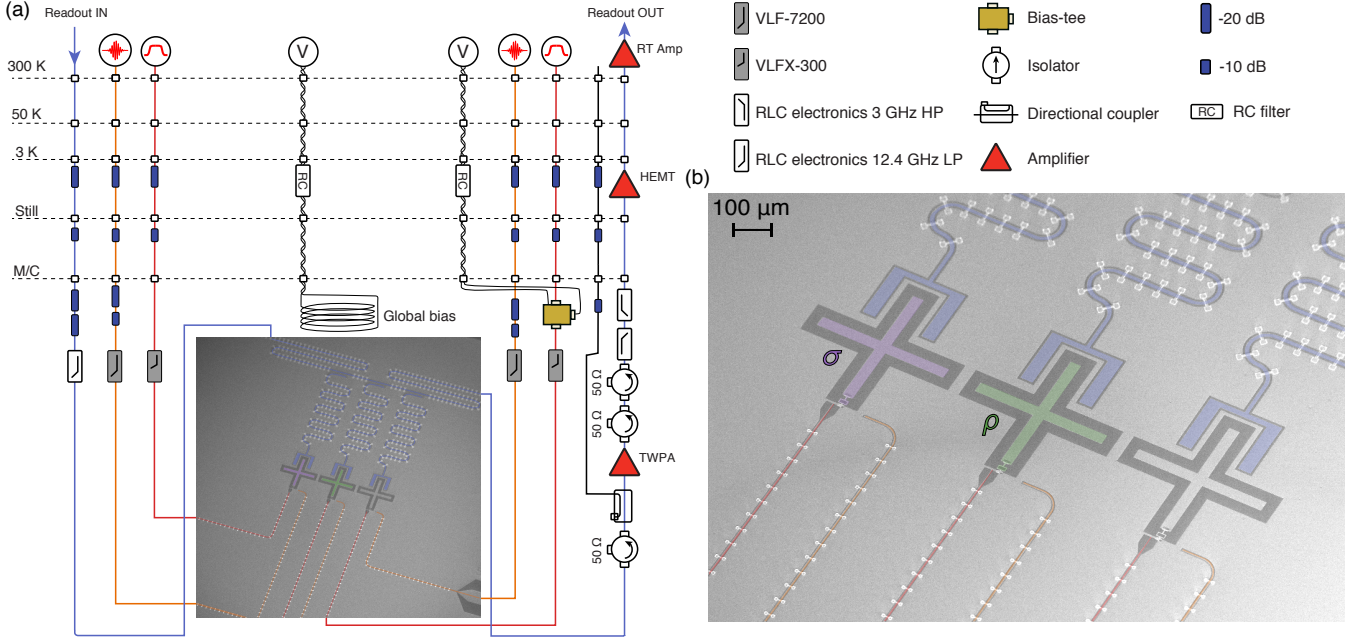


FIG. S1. (a) Schematic of readout- and control-wiring used for these experiments. The microwave line of qubit 3 is used to drive single-qubit gates on qubit 2. (b) SEM picture of identically fabricated device to the processor used in this work.

Parameter	Qubit 1 (σ , target)	Qubit 2 (ρ , instruction)
Idling frequency, $\omega_i/2\pi$	4.748 GHz	4.225 GHz
Anharmonicity, $\eta/2\pi$	-175 MHz	-190 MHz
Coupling strength, $g/2\pi$	10.6 MHz	
Readout resonator frequency, $f_i/2\pi$	7.251 GHz	7.285 GHz
Junction asymmetry	1:5	1:10
Relaxation time at idling point, T_1	23 μs	39 μs
Coherence time at idling point, T_{2R}	13 μs	25 μs
Effective relaxation time undergoing CZ trajectory, \tilde{T}_1	$\approx 17 \mu\text{s}$	(same as idling)
Effective coherence time undergoing CZ trajectory, \tilde{T}_{2R}	$\approx 5 \mu\text{s}$	(same as idling)
Single-qubit gate time, t_{1qb}	30 ns	30 ns
Two-qubit gate time, t_{CZ}	60 ns	

TABLE S1. Parameters of the two qubits used in this work. See text for details of the definition of \tilde{T}_1 and \tilde{T}_{2R} .

qubits used for the experiments in the main text. The measured lifetime T_1 and Ramsey coherence time T_{2R} exhibit temporal fluctuations, consistent with other reports [S4, S5].

For a qubit undergoing frequency modulation (*e.g.* to implement the CZ gate), frequency-dependent T_1 (and T_{2R}) variations mean that the static coherence times do not necessarily set the relevant limiting time-scale for the qubits [S4]. To account for the frequency-dependent variations in coherence as the target qubit undergoes the CZ trajectory, we employ an *effective* T_1 (T_{2R}) parameter, denoted \tilde{T}_1 (\tilde{T}_{2R}). These effective coherence times take into account any frequency-dependent variations of coherence as the qubit frequency undergoes the trajectory to enact a CZ gate. The effective coherence times are used in simulations of the device performance during two-qubit gates (see Appendix I). Since the frequency of qubit 2 is fixed during the CZ gate, its effective coherence times are identical to the idling coherence times.

Figure S2(a) shows an example measurement of \tilde{T}_1 . We prepare the state $|10\rangle$ (an eigenstate of CZ), apply n CZ gates in sequence, and measure the probability of staying in the $|10\rangle$ state. The exponential decay is fitted and we find a characteristic number of gates, $n_{\tilde{T}_1} \approx 264$. The CZ gate-time is 60 ns, and we use a 5 ns spacing between each pulse, leading to an effective decay time $\tilde{T}_1 = n_{\tilde{T}_1} \cdot t_{CZ} \approx 17 \mu\text{s}$.

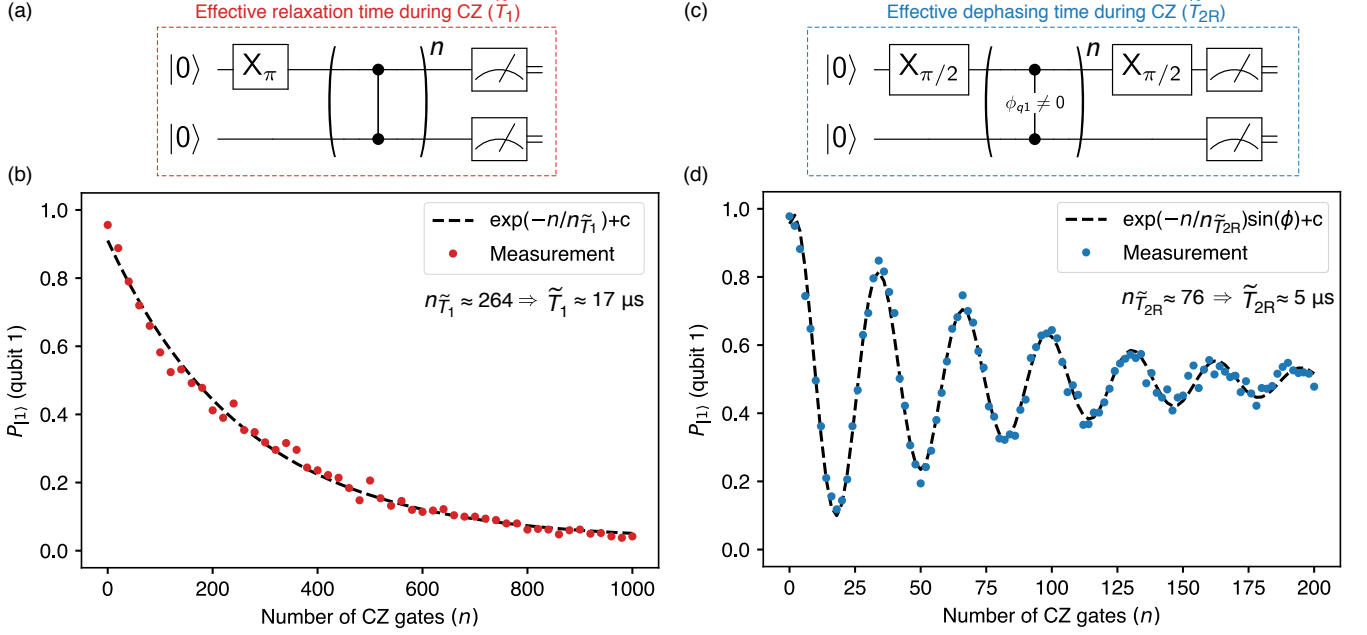


FIG. S2. (a) Measurement circuit to extract effective T_1 -like decay time, denoted \tilde{T}_1 . (b) Probability of measuring qubit 1 in the excited state, as the number of CZ gates is increased. The number $n_{\tilde{T}_1}$ sets a characteristic gate number, which can be converted into a characteristic time, \tilde{T}_1 . (c) Measurement circuit to extract effective T_{2R} -like decay time, denoted \tilde{T}_{2R} . We essentially perform a Ramsey measurement, but interleave CZ gates. (d) Probability of measuring qubit 1 in the excited state, as the number of CZ gates is increased. The number $n_{\tilde{T}_{2R}}$ gives the effective coherence time $\tilde{T}_{2R} \approx 5 \mu s$.

Similarly, to measure the effective coherence time, \tilde{T}_{2R} we prepare the $|+0\rangle$ state, apply n CZ gates and apply a final $X_{\pi/2}$ pulse. Unlike a Ramsey measurement, where we would idle between the $X_{\pi/2}$ pulses, we performed back-to-back CZ gates, effectively aggregating decoherence effects over the full frequency range of the CZ gate. To ensure an oscillatory behavior, a small single-qubit phase error is added ($\phi_{q1} \neq 0$), equivalent to performing a detuned Ramsey experiment. Fitting an exponentially damped sine function gives a characteristic decay number $n_{\tilde{T}_{2R}} \approx 76$ CZ gates. We again estimate the effective coherence time as $\tilde{T}_{2R} = n_{\tilde{T}_{2R}} \cdot t_{CZ} \approx 5 \mu s$.

Appendix B: Algorithmic error in DME_N

In this section we show that the algorithmic error in $DME_N(\rho, N, \theta)$ (the version of DME in which the instruction state is refreshed with a new, perfect copy after each Trotter step) may be modeled as an amplitude damping channel and derive its scaling with the parameters of the algorithm. We do so first for a specific instruction state, and then generalize to an arbitrary instruction. Throughout we use $\hat{\sigma}_i$ to indicate the corresponding Pauli matrix.

Suppose that we have instruction and target qubits initially in states ρ and σ respectively, and apply the operation $e^{-i\text{SWAP}\delta}$ to the joint state $\rho \otimes \sigma$. We will first consider the special case in which $\rho = |0\rangle\langle 0|$ and then show how this generalizes to an arbitrary state. The effect of the δSWAP on the target qubit is given by the quantum channel

$$\mathcal{E}_{\delta\text{SWAP}}^{\rho=|0\rangle\langle 0|}(\sigma) = \text{Tr}_\rho \left(e^{-i\text{SWAP}\delta} \left[\sigma \otimes |0\rangle\langle 0| \right] e^{i\text{SWAP}\delta} \right), \quad (\text{S1})$$

Next, we use the fact that

$$e^{i\text{SWAP}\delta} = \cos(\delta)\hat{\sigma}_{11} + i\sin(\delta)\text{SWAP}, \quad (\text{S2})$$

which follows from the fact that $\text{SWAP}^2 = \hat{\sigma}_{11}$ where $\hat{\sigma}_{11}$ is the two-qubit identity matrix. Using this together with the identity $\text{Tr}_\rho(\text{SWAP}(X \otimes Y)) = YX$ (where Tr_ρ is a partial trace over the second subsystem) we find

$$\mathcal{E}_{\delta\text{SWAP}}^{\rho=|0\rangle\langle 0|}(\sigma) = \cos^2(\delta)\sigma + i\cos(\delta)\sin(\delta)[\sigma, |0\rangle\langle 0|] + \sin^2(\delta)|0\rangle\langle 0|. \quad (\text{S3})$$

Using the matrix representation of σ in the $\{|0\rangle, |1\rangle\}$ basis, we find that σ transforms as

$$\begin{pmatrix} \sigma'_{00} & \sigma'_{01} \\ \sigma'_{10} & \sigma'_{11} \end{pmatrix} = \begin{pmatrix} \sigma_{00} + \sigma_{11} \sin^2(\delta) & \cos \delta e^{-i\delta} \sigma_{01} \\ \cos \delta e^{+i\delta} \sigma_{10} & \sigma_{11} \cos^2(\delta) \end{pmatrix} \quad (\text{S4})$$

where $\sigma_{ij} = \langle i|\sigma|j\rangle$ as measured in the $\{|0\rangle, |1\rangle\}$ basis. The channel that implements this transformation has a simple interpretation as the composition of a rotation and an amplitude decay.

Let

$$\mathcal{U}_\delta^{\rho=|0\rangle\langle 0|}(\cdot) = e^{-i\delta|0\rangle\langle 0|}(\cdot)e^{i\delta|0\rangle\langle 0|} = e^{-i\frac{\delta}{2}\hat{\sigma}_z}(\cdot)e^{+i\frac{\delta}{2}\hat{\sigma}_z} \quad (\text{S5})$$

be the superoperator corresponding to the unitary $e^{-i\delta|0\rangle\langle 0|}$, or equivalently, the superoperator corresponding to the rotation by angle δ around z axis. Also, let \mathcal{A}_p be the amplitude damping channel described by the Kraus decomposition

$$\mathcal{A}_p(\sigma) = A_1\sigma A_1^\dagger + A_2\sigma A_2^\dagger \quad (\text{S6})$$

where (see also Eq. S2)

$$A_1 = \begin{pmatrix} 1 & 0 \\ 0 & \sqrt{1-p} \end{pmatrix}, \quad A_2 = \begin{pmatrix} 0 & \sqrt{p} \\ 0 & 0 \end{pmatrix}. \quad (\text{S7})$$

This amplitude damping channel describes the process in which the system in state $|1\rangle$ decays to state $|0\rangle$ with probability p . It can be shown that the amplitude damping channel satisfies the condition

$$\mathcal{A}_p \circ \mathcal{U}_\delta = \mathcal{U}_\delta \circ \mathcal{A}_p \quad (\text{S8})$$

for all $\theta \in [0, 2\pi)$. This equality implies that the action of this channel is invariant under rotations around z axis.

Then, using Eq. (S4) one can show that

$$\mathcal{E}_{\delta\text{SWAP}}^{\rho=|0\rangle\langle 0|}(\sigma) = \mathcal{A}_{\sin^2(\delta)} \circ \mathcal{U}_\delta(\sigma) = \mathcal{U}_\delta \circ \mathcal{A}_{\sin^2(\delta)}(\sigma) \quad (\text{S9})$$

The overall effect of one Trotter step of DME_N can therefore be understood as the following: (i) Applying the unitary $e^{-i\delta|0\rangle\langle 0|}$ to the system σ , followed by (ii) applying the amplitude damping channel $\mathcal{A}_{\sin^2 \delta}$ to the system σ . Note that because of the condition in Eq. (S8), by flipping the order of steps (i) and (ii) we get exactly the same final state.

Now suppose we repeat the above operation N times. That is we prepare the instruction qubit in state $\rho = |0\rangle\langle 0|$, couple it to σ via the unitary $e^{-i\text{SWAP}\delta}$, then discard the instruction qubit and prepare it again in state $|0\rangle\langle 0|$, and repeat the above procedure with N different copies of ρ . Then, using Eq. (S8) one can show that, given an initial state σ , the final state of the target system will be

$$\left[\mathcal{E}_{\delta\text{SWAP}}^{\rho=|0\rangle\langle 0|} \right]^N(\sigma) = [\mathcal{A}_{\sin^2(\delta)} \circ \mathcal{U}_\delta]^N(\sigma) = \mathcal{A}_{\sin^2(\delta)}^N \circ \mathcal{U}_{N\delta}(\sigma). \quad (\text{S10})$$

Since amplitude damping channels are closed under composition, we see that

$$\mathcal{A}_{\sin^2(\delta)}^N = \mathcal{A}_{1-\cos^{2N}(\delta)}. \quad (\text{S11})$$

Therefore, the overall effect on the target system is equivalent to applying the perfect unitary $e^{-iN\delta|0\rangle\langle 0|}$, and then applying the amplitude damping channel $\mathcal{A}_{1-\cos^{2N}(\delta)}$.

Now, suppose in the above procedure, instead of state $|0\rangle\langle 0|$ we prepare the instruction qubit in state $|\phi\rangle\langle\phi| = V|0\rangle\langle 0|V^\dagger$, where V is an arbitrary unitary. Then, using the fact that $\text{SWAP}(V \otimes V') = (V' \otimes V)\text{SWAP}$, one can show that the overall effect of this transformation on the target system can be described as a unitary rotation $e^{-iN\delta|\phi\rangle\langle\phi|}$ followed by an amplitude damping channel in the basis defined by state $|\phi\rangle$ and its orthogonal state.

To translate explicitly to the language of the main text, let $\delta = \theta/N$ and $\rho = |\phi\rangle\langle\phi|$, and use the above procedure to implement the unitary $e^{-i\rho\theta}$ on the target system σ , using N copies of the instruction state ρ . From Eq. (S11) we find that the overall error in this procedure is determined by the probability $p_N = 1 - \cos^{2N}(\delta)$. Then, for $\delta \in (0, 2\pi]$ and $N \gg 1$ we have

$$p_N = 1 - \cos^{2N}\left(\frac{\theta}{N}\right) \approx 1 - e^{-\frac{\theta^2}{N}} \approx \frac{\theta^2}{N}, \quad \text{for large } N \quad (\text{S12})$$

In the limit of large N , this corresponds to an algorithmic error for the DME_N algorithm of $\mathcal{O}(\theta^2/N)$, as quoted in the main text Eq. (2).

Appendix C: Algorithmic error due to SQM

Here we provide an intuitive picture for the simulated quantum measurement (SQM) operation as well as a formal proof of the modified algorithmic error bound in Eq. (4) of the main paper.

We will build the intuition for this section by returning to the concrete example from Appendix B, *i.e.* the instruction qubit prepared in $\rho = |0\rangle\langle 0|$. We will also suppose that the target qubit is prepared in an orthogonal state, say, $\sigma = |+i\rangle\langle +i|$ (which is an eigenstate of the Pauli matrix $\hat{\sigma}_Y$). Since δSWAP is a symmetric operation by the logic in Appendix B the state of ρ following a small δSWAP interaction is given by a rotation about the y -axis followed by an amplitude damping channel (which we will neglect for the moment). In this case, the state of the instruction qubit becomes

$$\rho' = \begin{pmatrix} \cos^2(\delta) & -\cos(\delta)\sin(\delta) \\ -\cos(\delta)\sin(\delta) & \sin^2(\delta) \end{pmatrix} \quad (\text{S1})$$

The trace distance between ρ and ρ' is of order $|\delta|$. However, if we measure-and-forget the state of the instruction qubit in the basis of its original polarization (*i.e.* the z -basis), the coherent off-diagonal components of the density matrix are dephased and we are left with

$$\rho'' = \begin{pmatrix} \cos^2(\delta) & 0 \\ 0 & \sin^2(\delta) \end{pmatrix} \quad (\text{S2})$$

The trace distance between ρ'' and ρ is of order δ^2 . Because DME operates in the $\delta \ll 1$ regime, we have $\delta^2 \ll \delta$. Measuring-and-forgetting therefore leaves the instruction qubit in a slightly perturbed state that is closer to that of the initial state ρ .

The intuition developed for $\rho = |0\rangle\langle 0|$ extends naturally to an arbitrary initial state $\rho = |\nu_{\parallel}\rangle\langle \nu_{\parallel}|$, in a basis defined by $\nu = \{|\nu_{\parallel}\rangle, |\nu_{\perp}\rangle\}$. A small arbitrary rotation will result in the state

$$\rho' = \cos^2(\beta) |\nu_{\parallel}\rangle\langle \nu_{\parallel}| + \sin^2(\beta) |\nu_{\perp}\rangle\langle \nu_{\perp}| + \cos(\beta)\sin(\beta) (e^{i\phi} |\nu_{\parallel}\rangle\langle \nu_{\perp}| + e^{-i\phi} |\nu_{\perp}\rangle\langle \nu_{\parallel}|), \quad (\text{S3})$$

where β and ϕ generically parameterize the rotation. A measurement in the basis ν dephases the off-diagonal elements in this basis, leaving

$$\rho'' = \cos^2(\beta) |\nu_{\parallel}\rangle\langle \nu_{\parallel}| + \sin^2(\beta) |\nu_{\perp}\rangle\langle \nu_{\perp}| \quad (\text{S4})$$

which is closer than ρ' to ρ by a factor of $|\beta|$.

Performing a physical measurement along an arbitrary axis ν generically would require *i*) rotating ν onto the z -axis, *ii*) performing a projective readout, and *iii*) rotating back to the original axis. All of these steps require finite clock time: single-qubit gates (measurements) typically require tens (hundreds) of nanoseconds to complete. We would like to avoid this significant experimental overhead while still maintaining the ability to partially restore the instruction qubit to its initial state. Instead of physically performing the measurement, we can apply the unitaries $\{\hat{\sigma}_1, \hat{\sigma}_{\nu}\}$ with equal probabilities, where $\hat{\sigma}_{\nu} = \hat{n}_{\parallel} \cdot (\hat{\sigma}_X, \hat{\sigma}_Y, \hat{\sigma}_Z)$ and \hat{n}_{\parallel} is a unit vector parallel to ρ . Such protocols may be equivalently thought of as an approach to turning a coherent error into an incoherent error along a known axis. This protocol is the simulated quantum measurement (SQM) operation used in the main paper.

When averaged over many iterations, the randomized SQM operation dephases the system in the ν basis, just as in Eq. (S3)-(S4). Assuming the instruction qubit is initially in state ρ' , it turns out that the resulting state is the same for measurement and random gate application, *i.e.*

$$\frac{|\nu_{\parallel}\rangle\langle \nu_{\parallel}| \rho' |\nu_{\parallel}\rangle\langle \nu_{\parallel}| + |\nu_{\perp}\rangle\langle \nu_{\perp}| \rho' |\nu_{\perp}\rangle\langle \nu_{\perp}|}{2} = \frac{\hat{\sigma}_1 \rho' \hat{\sigma}_1 + \hat{\sigma}_{\nu} \rho' \hat{\sigma}_{\nu}}{2} = \frac{1}{2\pi} \int_0^{2\pi} d\gamma e^{-i\gamma \hat{\sigma}_{\nu}} \rho' e^{i\gamma \hat{\sigma}_{\nu}}. \quad (\text{S5})$$

These three terms represent respectively measuring-and-forgetting, random gate application, and phase randomization. Their equivalence can be understood more formally from the standpoint of the stochastic master equation, to which Ref. [S6] provides an accessible introduction. This approach is also related to the Quantum Zeno Effect, in which persistent measurement along an axis of interest “pins” the qubit state to that axis by continuously dephasing any rotations away from it [S7].

Finally, we calculate the additional error introduced to the DME algorithm by the use of SQM. For this, we return to the specific case where $\rho = |0\rangle\langle 0|$ (though this also generalizes to arbitrary ρ). As in Appendix B, we apply the

unitary $e^{-i\text{SWAP}\delta}$ to the joint state $\sigma \otimes |0\rangle\langle 0|$, and then randomly apply one of the unitaries $\{\hat{\sigma}_1, \hat{\sigma}_Z\}$ to the instruction qubit. Then, it can be shown that the total state of instruction and target qubit is given by

$$\begin{aligned} & \frac{1}{2} \left(e^{-i\text{SWAP}\delta} \left[\sigma \otimes |0\rangle\langle 0| \right] e^{i\text{SWAP}\delta} + (\hat{\sigma}_1 \otimes \hat{\sigma}_Z) e^{-i\text{SWAP}\delta} \left[\sigma \otimes |0\rangle\langle 0| \right] e^{i\text{SWAP}\delta} (\hat{\sigma}_1 \otimes \hat{\sigma}_Z) \right) \\ &= \underbrace{\mathcal{E}_{\delta\text{SWAP}}^{\rho=|0\rangle\langle 0|}(\sigma) \otimes |0\rangle\langle 0|}_{\text{DME}_N} - \underbrace{\sin^2(\delta) \langle 1|\sigma|1 \rangle \left[|0\rangle\langle 0| \otimes \hat{\sigma}_Z \right]}_{\text{SQM error}}, \end{aligned} \quad (\text{S6})$$

where $\mathcal{E}_{\delta\text{SWAP}}^{\rho=|0\rangle\langle 0|}(\sigma)$ is the quantum channel defined in Eq. (S9). Note that the first term, $\mathcal{E}_{\delta\text{SWAP}}^{\rho=|0\rangle\langle 0|}(\sigma) \otimes |0\rangle\langle 0|$ is exactly the desired state which can be used for the next round of DME. On the other hand, the second term $\sin^2(\delta) \langle 1|\sigma|1 \rangle \left[|0\rangle\langle 0| \otimes \hat{\sigma}_Z \right]$ can be treated as an error. To find the contribution of this term in the total error, we use the fact that the trace-norm is non-increasing under any trace-preserving quantum operation \mathcal{F} : $\|\mathcal{F}(X)\|_{\text{tr}} \leq \|X\|_{\text{tr}}$, where $\|\cdot\|_{\text{tr}}$ is trace norm, *i.e.* sum of the absolute value of the eigenvalues of the operator.

For the second term in Eq. (S6) we have

$$\left\| \sin^2(\delta) \langle 1|\sigma|1 \rangle \left[|0\rangle\langle 0| \otimes \hat{\sigma}_Z \right] \right\|_{\text{tr}} = 2 \sin^2(\delta) \langle 1|\sigma|1 \rangle \leq 2 \sin^2(\delta). \quad (\text{S7})$$

Therefore, the additional error introduced by each application of SQM is bounded by $2 \sin^2(\delta)$.

Repeating this process N times, and using the triangle inequality for the trace norm, we find that the distance between the final total system state and the state produced by DME_N is bounded by $2N \sin^2(\delta)$. Choosing $\delta = \theta/N$, we find that the overall additional error introduced by the use of SQM is bounded by

$$2N \sin^2(\delta) = 2N \sin^2\left(\frac{\theta}{N}\right) \leq \frac{2\theta^2}{N}. \quad (\text{S8})$$

The right hand side of Eq. (S8) is the error contribution cited in the main text Eq. (4).

Appendix D: Details of the compilation

A δSWAP could be realized by implementing the quantum version of xor-swapping, but only swapping part of the state. To see this, recall that a full SWAP can be implemented by [S8]

$$\text{SWAP} = \begin{array}{c} \text{---} \bullet \text{---} \oplus \text{---} \bullet \text{---} \\ | \quad | \quad | \\ \text{---} \oplus \text{---} \bullet \text{---} \oplus \text{---} \end{array} = \begin{pmatrix} 1 & 0 & 0 & 0 \\ 0 & 0 & 1 & 0 \\ 0 & 1 & 0 & 0 \\ 0 & 0 & 0 & 1 \end{pmatrix}. \quad (\text{S1})$$

From this construction, then, an arbitrary-strength SWAP interaction can be generated. One version of a δSWAP circuit is given below;

$$\delta\text{SWAP} := \begin{array}{c} \text{---} \bullet \text{---} \boxed{\text{H}} \text{---} \bullet \text{---} \boxed{\text{H}} \text{---} \bullet \text{---} \\ | \quad | \quad | \quad | \quad | \\ \text{---} \oplus \text{---} \bullet \text{---} \oplus \text{---} \end{array} = \begin{pmatrix} 1 & 0 & 0 & 0 \\ 0 & (1 + e^{i2\delta})/2 & (1 - e^{i2\delta})/2 & 0 \\ 0 & (1 - e^{i2\delta})/2 & (1 + e^{i2\delta})/2 & 0 \\ 0 & 0 & 0 & 1 \end{pmatrix}. \quad (\text{S2})$$

where

$$\begin{array}{c} \text{---} \bullet \text{---} \\ | \\ \text{---} \bullet \text{---} \end{array} \stackrel{\delta}{=} \begin{pmatrix} 1 & 0 & 0 & 0 \\ 0 & 1 & 0 & 0 \\ 0 & 0 & 1 & 0 \\ 0 & 0 & 0 & e^{-i\delta} \end{pmatrix} := \text{CZ}_\delta \quad (\text{S3})$$

is a partial CZ gate. However, such a construction would rely on tuning up high fidelity versions of CZ_δ for each value of δ [S9]. Since we rely on numerical optimization based on Clifford randomized benchmarking (Appendix E), achieving ‘last-mile’ optimization using Clifford RB [S10] would require constructing the set of Cliffords out of CZ_δ ,

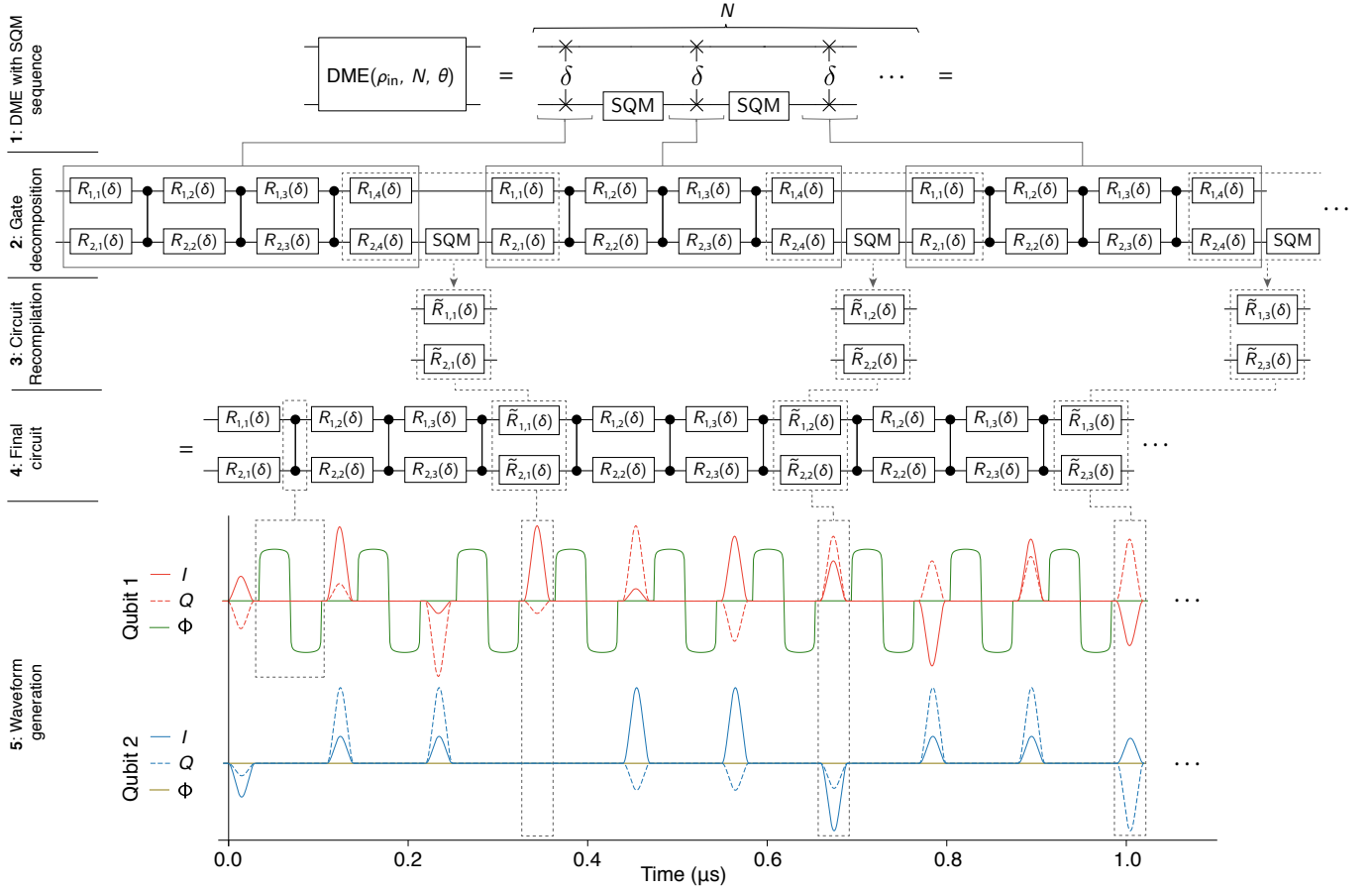


FIG. S3. **Row 1.** The density matrix exponentiation algorithm implemented using partial SWAP operations and the simulated quantum measurement (SQM) gate. **Row 2.** Decomposing each δ SWAP according to Eq. (S5). Each substep at this step requires 8 layers of gates (7 for δ SWAP decomposition and 1 for SQM). **Row 3.** The three layers of single-qubit gates stemming from the the end of the δ SWAP of step n , followed by SQM, and the first layer of single-qubit gates in δ SWAP of step $n + 1$ can be recompiled into a single layer. **Row 4.** The recompiled gates are reinserted into the algorithm result in the optimal structure of exactly one CZ gate, followed by a single layer of single-qubit gates. **Row 5.** Example waveform output to the I, Q (x, y) ports and the flux tuning pulse (labeled Φ) implementing the ‘NetZero’ waveform used to implement the CZ gate [S11, S12].

again for each value of δ . Such a strategy quickly becomes infeasible as the value of δ deviates significantly from π , requiring many CZ_δ gates to form a single two-qubit Clifford gate.

One way around this issue of tuning up high-fidelity two-qubit gates for each δ value would be to use a second compilation pass, *e.g.* by using the decomposition,

$$\delta = \begin{array}{c} \bullet \\ \delta \\ \bullet \end{array} = \begin{array}{c} \boxed{Z_{\delta/2}} \\ \boxed{Z_{\delta/2}} \oplus \boxed{Z_{-\delta/2}} \end{array} \quad (S4)$$

However, such an approach would introduce *two* CZ gates for each CZ_δ gate, adding significant circuit depth overhead.

Alternatively, we use a more generalized and gate-efficient approach. We utilize the fact that any two-qubit gate can be decomposed into a circuit with the structure [S8, S13]

$$U_{2QB} = \begin{array}{c} \boxed{R_{1,1}} \bullet \boxed{R_{1,2}} \bullet \boxed{R_{1,3}} \bullet \boxed{R_{1,4}} \\ \boxed{R_{2,1}} \oplus \boxed{R_{2,2}} \oplus \boxed{R_{2,3}} \oplus \boxed{R_{2,4}} \end{array} \quad (S5)$$

Where $R_{i,j}$ is a single-qubit gate acting on qubit i at moment j in the circuit and \bullet is the CNOT gate with qubit 2 as the target.

By using the identity


(S6)

and absorbing the Hadamard gates (H) into the neighboring single-qubit gates, the circuit in Eq. (S5) becomes identical to the circuit in Eq. (5) in the main text.

We use the open-source software `Cirq` [S14] to determine the settings of the single-qubit gates for each value of δ . The single-qubit rotations around the x, y axes are decomposed according to $R_Z(-\varphi)R_X(\theta)R_Z(\varphi)$ (the `PhasedXPowGate` in `Cirq`) and the R_Z rotations are performed virtually [S15]. The δ SWAP is implemented using the `SwapPowGate` function in `Cirq` (the `SwapPowGate` has a factor of 2 difference, relative to our definition of δ SWAP). Thus, we are able to compose a unique composite gate sequence for each δ SWAP relying only on high-fidelity single- and two-qubit gates (Appendix E).

To construct the full $\text{DME}(\rho, N, \theta)$ circuit, we append N copies of the compiled δ SWAP gate using $\delta = \theta/N$, interleaving the requisite SQM_ν on qubit 2 (the instruction qubit, ρ) to emulate the effect of measurements (see main text and Appendix C). Rows 1 and 2 in Figure S3 shows the generic structure and gate decomposition of our implementation of DME. The final layer of single-qubit gates in the δ SWAP at step n can be recompiled together with the SQM_ν , and the first layer of single-qubit gates in the δ SWAP at step $n + 1$. We again use `Cirq` to slice out these three layers (Row 2 in Figure S3) of single-qubit gates, recompile them into a single layer (Row 3 in Figure S3), and reinsert them (Row 4 in Figure S3). Finally, in Row 5 of Figure S3 we show an example waveform output from our signal generation software, implementing the first $n = 3$ steps in a $N = 5$ DME program.

Our compilation has several features that enable it to achieve high algorithmic fidelity at significant circuit depth. First, it relies upon a restricted set of gates that are readily characterized and numerically optimized (Appendix E 1 and Appendix E 2). In particular, the final compiled circuit has a regular structure (each CZ is followed by exactly one layer of single-qubit gates), amenable to generic tuneup protocols for reducing coherent error buildup (Appendix E 3).

Appendix E: Benchmarking qubit operations

We use a combination of metrics to quantify the quality (fidelity) of the qubit operations during the algorithm. These techniques include single- and two-qubit randomized benchmarking (RB) as well as novel techniques for amplifying and correcting coherent errors.

1. Single qubit gates: Randomized benchmarking

Figure S4 shows single-qubit Clifford randomized benchmarking of the single-qubit operations on both qubit 1 (Figure S4(b)) and 2 (Figure S4(c)). Each trace averages 25 randomizations of the RB circuit [S16]. The reference curves (circuit diagram in Figure S4(a), grey dashed box) are fit to a function of the form

$$f(m) = Ap^m + B \quad (\text{S1})$$

For the one qubit Clifford reference curve we denote p by p_r . The average error per Clifford gate \mathcal{C} can be calculated as

$$\epsilon_r = \frac{1}{2}(1 - p_r) \quad (\text{S2})$$

The error associated with a specific single-qubit gate is extracted by performing interleaved randomized benchmarking (IRB). We fit the IRB data (circuit diagram in Figure S4(a), red dashed box) for the relevant gate (denoted g) to Eq. S1 (denoting by p_g the p value for gate g). Then normalizing the error rate to the one qubit Clifford reference [S17],

$$\epsilon_g = \frac{1}{2}(1 - p_g/p_r), \quad (\text{S3})$$

Using this procedure we find an average Clifford gate fidelity ($F_r = 1 - \epsilon_r$) of 0.9987 for qubit 1 and 0.9987 for qubit 2. The average gate fidelity (*i.e.* $\bar{F} = \langle 1 - \epsilon \rangle_g$) over all single-qubit gates is 0.9991 for qubit 1 and 0.9994 for qubit 2.

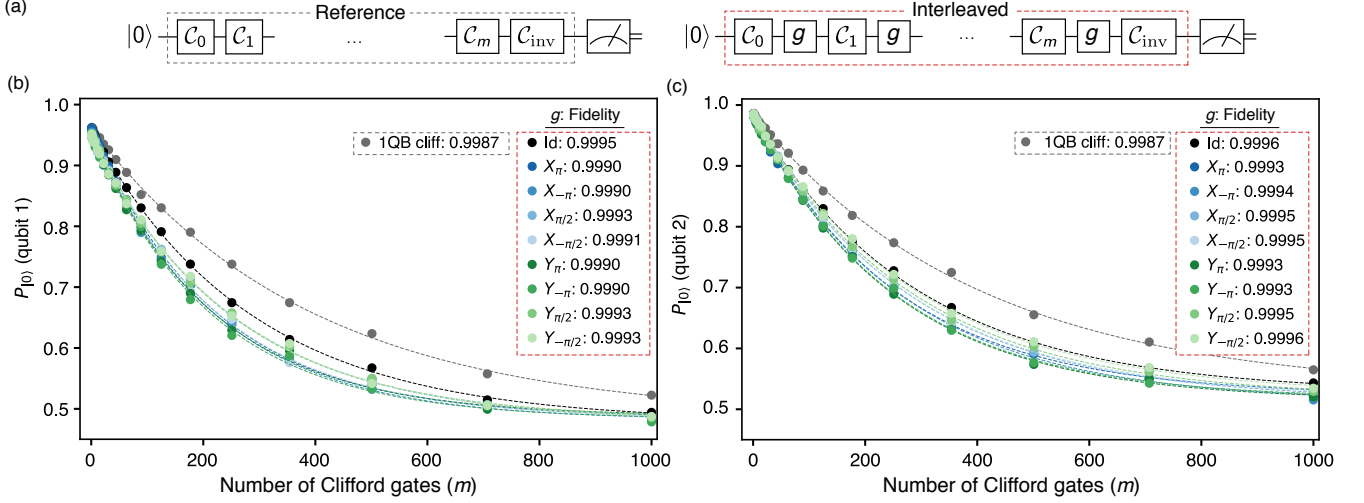


FIG. S4. (a) Circuit diagrams for measuring the reference curve (gray dashed box) and interleaved curve for a single qubit gate g (red dashed box) relevant for Clifford randomized benchmarking for a single qubit. (b) [(c)] Results for reference (gray) and interleaved (varying colors, for each gate) randomized benchmarking for qubit 1 [qubit 2].

2. Two qubit gates: Randomized benchmarking

To assess the two-qubit gate fidelity we again first use randomized benchmarking. The protocol is identical to the single-qubit case, except we measure the probability of being in the $|00\rangle$ state after the sequence [S16]. We use 48 randomizations for both reference and interleaved measurements (circuits shown in Figure S5(a)). In Figure S5(b) we show the result of the RB and IRB measurements. The error bars are 1σ standard deviations of the output distribution of the 48 random circuits. The fit is again performed using Eq. (S1), and error margins are extracted using forward-propagation of weights based on the standard deviation at each m to ensure accurate error bounds. This is achieved using the `absolute_sigma` option of the Python `scipy.optimize.curve_fit` function. The two-qubit Clifford reference error rate is calculated similarly to Eq. (S2) (with p being the two-qubit Clifford reference value,

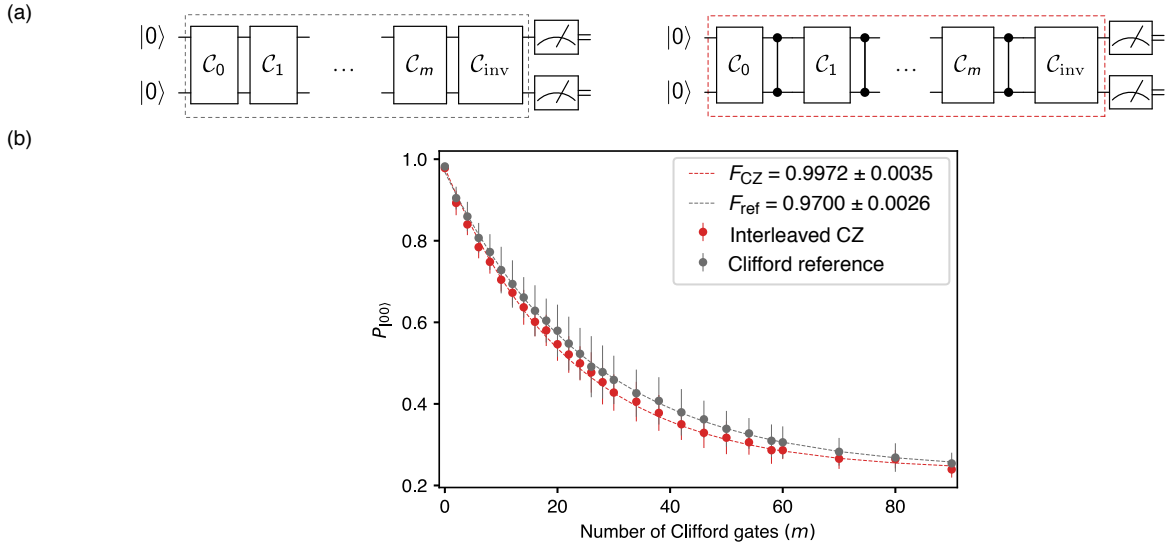


FIG. S5. (a) Gate sequences for measuring the two-qubit Clifford reference (gray dashed box) and interleaved CZ (red dashed box) RB numbers. (b) Example decay curve of $P_{|00\rangle}$ as the number of two-qubit Clifford gates (m) is increased. Each datapoint is averaged over $k = 48$ randomizations of the choice of Clifford gates. Error bars are 1σ standard deviations at each point from the 48 measurements, and fitting is performed using forward propagation of points weighted by their error bars.

denoted p_{2r}) but the error per Clifford is modified to

$$\epsilon_{2r} = \frac{3}{4}(1 - p_{2r}). \quad (\text{S4})$$

Then, ϵ_{CZ} is found by performing IRB and fitting the interleaved data to get p_{CZ} and normalizing to the 2QB reference error. Doing so, we find a CZ gate fidelity

$$F_{\text{CZ}} = 1 - \epsilon_{\text{CZ}} = 0.9972 \pm 0.0035. \quad (\text{S5})$$

To achieve ‘last-mile’ improvements in fidelity we use numerical optimization techniques to fine-tune parameters of the NetZero waveform, with the RB decay curve as a cost function [S10, S12].

3. Two qubit gates: Reducing small coherent errors

As practitioners of quantum computing have explored more complex circuits at greater depth and with more underlying structure, it has become evident that RB is a limited metric for the performance of a gate (see *e.g.* [S18–S20] and references therein). In particular, small coherent errors can cause disproportionately deleterious effects in algorithms with a repetitive structure (such as Trotterized algorithms), and RB is ill-suited to characterize such small coherent errors because it is designed to randomize over them.

To minimize the effects of coherent errors in the CZ gate, we implement a calibration technique which relies on process tomography of long strings of CZ gates (Figure S6). The general controlled-phase gate (denoted $\text{CZ}_{\phi_{01}, \phi_{10}, \phi_{11}}$) is given by

$$\text{CZ}_{\phi_{01}, \phi_{10}, \phi_{11}} = \begin{bmatrix} 1 & 0 & 0 & 0 \\ 0 & e^{-i\phi_{01}} & 0 & 0 \\ 0 & 0 & e^{-i\phi_{10}} & 0 \\ 0 & 0 & 0 & e^{-i\phi_{11}} \end{bmatrix} \quad (\text{S6})$$

If $\phi_{01} = \phi_{10} = 0$ and $\phi_{11} = \pi$ this produces the target CZ gate. However, for small deviations from these parameters it is still possible to achieve $\gtrsim 0.99$ randomized benchmarking fidelities. Since small phase deviations can compound

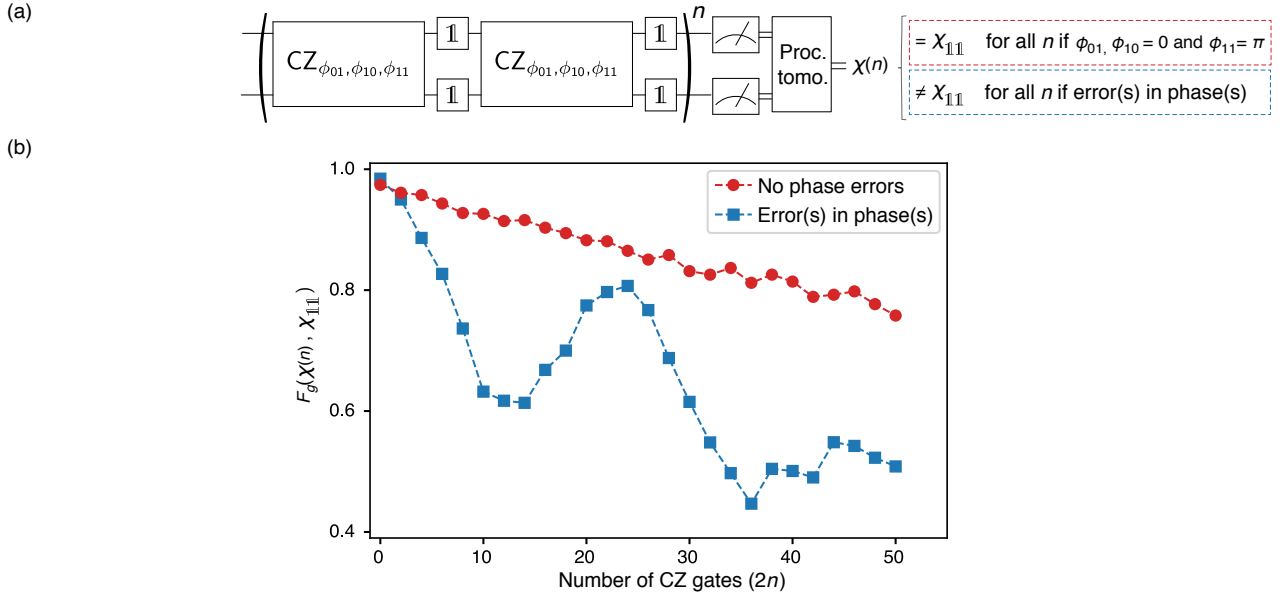


FIG. S6. (a) Gate sequence used to perform process tomography of a sequence of an even number of CZ gates, to get the chi-matrix $\chi(n)$, used to compare with the identity process map to infer coherent errors. The gate-sequence will nominally implement χ_{11} up to overall system decoherence (visible as the overall decrease of both the linear and oscillating measurements) if there are no phase errors in the $\text{CZ}_{\phi_{01}, \phi_{10}, \phi_{11}}$ gate. (b) The gate fidelity $F_g(\chi(n), \chi_{11})$ as the number of CZ gates ($2n$) is increased. With no phase errors in the CZ gate, F_g decreases monotonically. With a phase error in the CZ gate F_g will oscillate, with the period indicating the scale of the phase error.

to form larger errors – specifically in algorithms with a repeating pattern like DME or quantum error correction protocols – we have developed other calibration strategies to detect and correct such errors.

Our amplification protocol is comprised of implementing a circuit with two back-to-back blocks of $\text{CZ}_{\phi_{01}, \phi_{10}, \phi_{11}}$ followed by identity gates on both qubits designed to mimic the presence of single-qubit gates, see Figure S6(a). If the CZ gate contains no phase errors, this sequence produces an identity operation, irrespective of the number (n) of such two-CZ blocks applied. We perform two-qubit process tomography (see Appendix F) to extract the process matrix $\chi(n)$. We compare $\chi(n)$ to the process map of a two-qubit identity operation (χ_{11}) via the gate fidelity $F_g(\chi(n), \chi_{11})$ which is related to the process fidelity (defined in the main text) as

$$F_g(\chi, \chi') = \frac{dF_p(\chi, \chi') + 1}{d + 1} \quad (\text{S7})$$

where d is the dimensionality of the Hilbert space ($d = 4$ in the case of a two-qubit gate).

Figure S6(b) shows the gate fidelity of a circuit optimized to remove phase errors from the CZ gate (red circles), and one in which a CZ-gate *with* phase errors is used (blue squares). In the optimized case, the monotonic gate fidelity decay stems only from decoherence effects. However, in the presence of a coherent phase error, the gate fidelity oscillates with n . In this specific example, after roughly 25 CZ gates, the phase-error has effectively rotated by 2π , corresponding to an approximate per-step error of $2\pi/25 \approx 0.08\pi$ in one of the phases.

The evolution of the process maps in Figure S6 is useful both practically (for achieving higher performance gates) and scientifically (for understanding the limitations of RB). By examining the details of the process maps, we are able to infer in which of the parameters ϕ_{01} , ϕ_{10} or ϕ_{11} the error appeared, and to correct accordingly. This minor correction typically does not change the fidelity as measured with RB (except in the case of particularly egregious phase errors). From Figure S6(b) it is also clear that process tomography of a single CZ instance does not reveal the coherent error: the first datapoint for the sequence with phase errors has nearly identical fidelity to the optimized gate. Both of these facts are consistent with a growing understanding that RB may not be the optimal approach to identifying and correcting coherent errors in single- and multi-qubit gates. Finally, the identity gates are inserted between the CZ gates to as closely as possible mimic the generic optimal gate-sequence of a two-qubit algorithm, without exploiting any specific structure of an algorithm (see Appendix D for details on gate compilation).

In the data presented in the main paper, the combination of this tuneup strategy and compilation techniques of Appendix D was crucial: relying solely on maximizing RB fidelity of the CZ gate often yielded algorithmic results dominated by coherent error buildup that the RB missed.

Appendix F: Details of state and process tomography

Quantum state tomography is performed by taking advantage of independent single-shot readout of all four computational states $\{00, 01, 10, 11\}$. We first calibrate the measurement operators by building a matrix $\bar{\beta}$ that maps the two-qubit Pauli matrices $\hat{\sigma}_{11}$, $\hat{\sigma}_{1Z}$, $\hat{\sigma}_{Z1}$, and $\hat{\sigma}_{ZZ}$ onto the measurement probabilities p_{ij} :

$$\vec{p} = \bar{\beta} \vec{\sigma}, \quad (\text{S1})$$

where

$$\vec{p} \equiv \begin{pmatrix} p_{00} \\ p_{01} \\ p_{10} \\ p_{11} \end{pmatrix} \quad \text{and} \quad \vec{\sigma} \equiv \begin{pmatrix} \hat{\sigma}_{11} \\ \hat{\sigma}_{1Z} \\ \hat{\sigma}_{Z1} \\ \hat{\sigma}_{ZZ} \end{pmatrix} \quad (\text{S2})$$

The $\bar{\beta}$ matrix is calibrated using techniques drawn from Ref. [S21]; a full motivation and derivation of the technique can be found there. For a measurement of \vec{p} with perfect fidelity and no qubit decay during measurements, all components of $\bar{\beta}$ have amplitude 0.25; deviations from this amplitude correspond to a calibration of such measurement errors. We begin by calibrating the single-qubit $\bar{\beta}$ matrices, namely

$$\begin{pmatrix} p_0 \\ p_1 \end{pmatrix} = \begin{pmatrix} \beta_1^0 & \beta_Z^0 \\ \beta_1^1 & \beta_Z^1 \end{pmatrix} \begin{pmatrix} \hat{\sigma}_1 \\ \hat{\sigma}_Z \end{pmatrix} \quad (\text{S3})$$

by fitting Rabi oscillations in p_0 and p_1 for each qubit. Because the two-qubit probability vector \vec{p} is generated from correlations between single-qubit measurements, the two-qubit $\bar{\beta}$ matrix is given by the tensor product of the single-qubit matrices, *e.g.* $\bar{\beta} = \bar{\beta}_1 \otimes \bar{\beta}_2$.

An arbitrary 4×4 matrix, including a two-qubit density matrix ρ , may be mapped onto the Pauli basis according to

$$\rho = \sum_{i,j=\{1,X,Y,Z\}} c_{ij} \hat{\sigma}_{ij}. \quad (\text{S4})$$

The general 4×4 matrix of this form has sixteen degrees of freedom; trace normalization of a physical density matrix reduces this to fifteen. The native readout gives us access to the components of ρ contained in $\hat{\sigma}_Z$. We gain information about the other components by performing one of nine pre-measurement rotations drawn from:

$$R = R_1 \otimes R_2 \quad \text{where} \quad R_{1,2} = \begin{cases} R_Y(-\frac{\pi}{2}) & \text{mapping } \hat{\sigma}_X \mapsto \hat{\sigma}_Z \\ R_X(\frac{\pi}{2}) & \text{mapping } \hat{\sigma}_Y \mapsto \hat{\sigma}_Z \\ \mathbb{1} & \text{mapping } \hat{\sigma}_Z \mapsto \hat{\sigma}_Z \end{cases} \quad (\text{S5})$$

For data in Figure 2 (3, 4) in the main text we perform 2000 (500) single-shot measurements for each tomographic rotation in order to ensure accurate estimates of \vec{p} . Each of the nine rotation-and-measurement pairings provides four linearly independent measurements of a form similar to Eq. (S1), for a total of thirty-six equations that over-specify fifteen degrees of freedom. We perform maximum-likelihood estimation [S22] to derive the positive semi-definite Hermitian matrix that is most consistent with our combined measurement results.

Single-qubit density matrices in Figs. 2–3 of the main text are extracted by performing partial traces over the two-qubit density matrix calculated using the approach described above; the data in Figure 4 of the main text are drawn from single-qubit tomography performed on the target qubit using a similar protocol.

Single-qubit quantum process tomography, as presented in Figure 4 of the main text, is performed using standard techniques [S8]. The target qubit is sequentially prepared in four input states

$$\sigma_{\text{in}} = \{|0\rangle\langle 0|, |1\rangle\langle 1|, |+\rangle\langle +|, |i\rangle\langle i|\} \quad (\text{S6})$$

which span the single-qubit Hilbert space. These prepared states are then passed through the process $\text{DME}(\rho, N, \theta)$ and single-qubit state tomography is performed to extract the set of mappings $\{\sigma_{\text{in}} \xrightarrow{\text{DME}(\rho, N, \theta)} \sigma_{\text{out}}\}$. Linear combinations of these mappings provide the process map χ that reveals the effect of the quantum channel on an arbitrary input density matrix. We then employ techniques developed in Ref. [S23] to efficiently project χ onto the closest completely positive and trace-preserving (CPTP) mapping χ_{CPTP} , ensuring physicality of the process.

Appendix G: Details of bootstrap error analysis

We employ bootstrapping techniques to derive the uncertainty bounds in Figs. 3–4 of the main text. In principle, one could simply take a sample of many SQM randomizations and calculate the mean and uncertainty within that dataset. However, those error bars are not representative of the error in the DME protocol – rather, they represent the uncertainty of a protocol in which only a single SQM randomization is used to perform DME. As a result, these error bars are unphysically large, particularly at small N where the protocol chooses from one of only a few paths that have very different outcomes.

The true uncertainty of the DME protocol is captured by *i*) accumulating enough SQM samples to ensure sufficient randomizations (see Appendix H), *ii*) building density/process matrices from the average outcome of all these randomizations, and then *iii*) repeating this process many times with different randomizations to estimate the uncertainty. This is precisely what bootstrapping accomplishes [S24].

The following describes the protocol for extracting bootstrapped averages and uncertainties for Figure 3. For each data point representing a unique setting of $\text{DME}(\rho, N, \theta)$, we employ the following protocol:

1. For a given instantiation of the SQM gates, execute $\text{DME}(\rho, N, \theta)$ and perform two-qubit state tomography as described in Appendix F.
2. For r_{SQM} different instantiations of SQM gates, repeat step 1 to accumulate the experimental density matrices from which bootstrapped samples will be drawn.
3. Using sample-with-replacement, select n_{samp} samples from the r_{SQM} datasets and average the density matrices together. This represents a single bootstrapped density matrix.
4. Perform a partial trace over the instruction qubit to extract the reduced density matrix of the target system.
5. Calculate the state fidelity to the states of interest.
6. Repeat steps 3–5 a total of N_{samp} times to extract mean fidelities and 1σ uncertainties.

The bootstrapping protocol for generating process maps and process fidelities in Figure 4 is similar to that used for state tomography, but we lay it out here explicitly for completeness.

1. For a given instantiation of the SQM gates, prepare the target input states $\{\sigma_{\text{in}}\}$, apply $\text{DME}(\rho, N, \theta)$, and perform single-qubit state tomography to generate the mappings $\{\sigma_{\text{in}} \mapsto \sigma_{\text{out}}\}$ required for process tomography as described in Appendix F.
2. For r_{SQM} different instantiations of SQM gates, repeat step 1 to produce a set of $4 \times r_{\text{SQM}}$ single-qubit density matrices.
3. For each of the four σ_{in} , select an independent sample-with-replacement of n_{samp} σ_{out} instances and average together, leaving four averaged mappings $\{\sigma_{\text{in}} \mapsto \sigma_{\text{out}}\}$.
4. Calculate the process matrix using the averaged mappings $\sigma_{\text{in}} \mapsto \sigma_{\text{out}}$. This represents a single bootstrapped process matrix.
5. Calculate the process fidelity to the process of interest.
6. Repeat steps 3-5 a total of N_{samp} times to extract mean fidelities and 1σ uncertainties.

The values of r_{SQM} , n_{samp} , and N_{samp} are reported in Table S2. The number of SQM randomizations used for process tomography was limited by experimental time, due to the significant additional experimental overhead required for process tomography in comparison to state tomography, and due to the fact that in Figure 4 we characterize processes for six settings of ρ . The bootstrap sample size n_{samp} and number of bootstrap samples N_{samp} are chosen somewhat arbitrarily, as in all bootstrapping implementations, but are designed to ensure that each bootstrapped sample approaches a central limit with respect to the underlying SQM randomization.

Figure #	r_{SQM}	n_{samp}	N_{samp}
Figure 3	295	100	50
Figure 4	105	100	50

TABLE S2. Bootstrapping and SQM randomization details for Figure 3 and 4 in the main text.

Appendix H: Quantifying the impacts of finite SQM randomizations

To properly implement the probabilistic nature of the SQM operation we instantiate each DME circuit a number of times. Consider as an example the $N = 3$ version of the DME circuit from Figure 3,

$$\sigma \rightarrow \boxed{\text{DME}(|+i\rangle\langle +i|, 3, \pi/2)} \rightarrow \sigma_{\text{out}} = \begin{array}{c} \sigma \xrightarrow{\pi/6} \xrightarrow{\pi/6} \xrightarrow{\pi/6} \sigma_{\text{out}} \\ | + i \rangle \langle + i | \xrightarrow{\pi/6} \boxed{\text{SQM}_y} \xrightarrow{\pi/6} \boxed{\text{SQM}_y} \xrightarrow{\pi/6} \boxed{\text{SQM}_y} \end{array} \quad (\text{S1})$$

In this case, each SQM presents a random choice between applying $R_Y(\pi)$ or $\mathbb{1}$ at each occurrence. For an N step DME there are 2^N configurations of SQM gates. In the experiment it is infeasible to sample all 2^N realizations, and instead we sample a smaller number, denoted r . The circuits below show $r = 3$ random example realizations of the circuit,

$$\begin{array}{c} \xrightarrow{\pi/6} \xrightarrow{\pi/6} \xrightarrow{\pi/6} \\ \xrightarrow{\pi/6} \boxed{\mathbb{1}} \xrightarrow{\pi/6} \boxed{R_Y(\pi)} \xrightarrow{\pi/6} \boxed{\mathbb{1}} \end{array}, \quad \begin{array}{c} \xrightarrow{\pi/6} \xrightarrow{\pi/6} \xrightarrow{\pi/6} \\ \xrightarrow{\pi/6} \boxed{R_Y(\pi)} \xrightarrow{\pi/6} \boxed{R_Y(\pi)} \xrightarrow{\pi/6} \boxed{R_Y(\pi)} \end{array}, \quad \begin{array}{c} \xrightarrow{\pi/6} \xrightarrow{\pi/6} \xrightarrow{\pi/6} \\ \xrightarrow{\pi/6} \boxed{\mathbb{1}} \xrightarrow{\pi/6} \boxed{\mathbb{1}} \xrightarrow{\pi/6} \boxed{R_Y(\pi)} \end{array} \quad (\text{S2})$$

In the experiment, a total r_{SQM} of circuits are executed, providing a sample from which we can extract average properties (See Appendices F and G for details). The generic process for extracting average properties over r instantiations is sketched in Figure S7(a).

From the datasets used in the main paper, we can also explore algorithmic behavior as the randomizations of SQM increase toward the central limit. In Figure S7(b)-(d) we plot three relevant figures of merit as a function of r and N for the $\theta = \pi$ dataset of Figure 3 in the main text. Figure S7(b) shows the evolution of the state fidelity of the output state as a function of r . For all values of N we observe that after approximately ~ 50 randomizations the effect of introducing more circuits with random choices of SQM gates does not significantly alter the result. Figure S7(c)

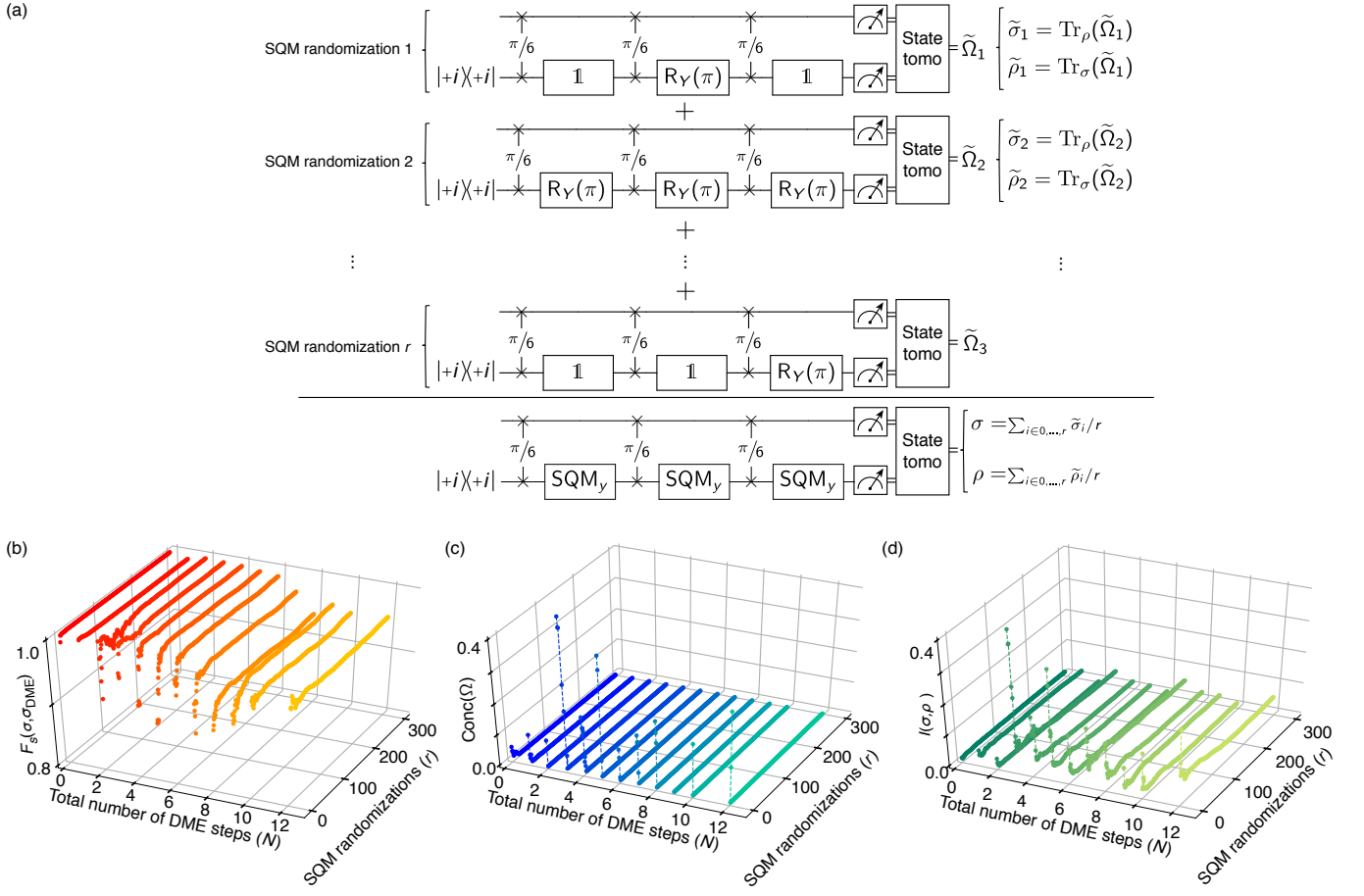


FIG. S7. (a) Schematic definition of experimental execution of a DME protocol using SQM operations. (b) The state fidelity between the measured output state and the result of ideal gates implementing DME, as the number of SQM randomizations are increased. (c) Concurrence in the two-qubit density matrix Ω (the combined state of the system), for increasing number of SQM randomizations. (d) The mutual information between the two subsystems σ and ρ , as more randomizations of SQM are used.

shows the concurrence of the two-qubit density matrix, a measurement of bi-partite entanglement in the system [S25]. After just a few randomizations $r > 10$, concurrence goes to zero, indicating that (quantum) correlations have been suppressed, as expected. There may also be classical correlations between the σ and ρ subsystems. In Figure S7(d) we therefore plot the mutual information $I(\sigma, \rho)$ between each subsystem, where

$$I_{\Omega}(\sigma, \rho) = S(\text{Tr}_{\sigma}(\Omega)) + S(\text{Tr}_{\rho}(\Omega)) - S(\Omega) \quad (\text{S3})$$

is the mutual information, and $S(\Omega) = -\text{Tr}(\Omega \ln \Omega)$ is the von Neumann entropy of the density matrix Ω . Here we again observe that after $r > 10$ any correlations between the subsystems are effectively removed.

Appendix I: Circuit simulation with noise

In order to show the qualitative consistency between the data in Figure 3 and a model of coherence-limited implementation of the DME protocol, we simulate the randomized DME circuits with added decoherence. We input a DME circuit generated by Cirq to a software tool that adds decoherence (amplitude damping and dephasing) channels corresponding to the identity for duration(s) of the preceding one- or two-qubit gate. An example of this procedure is shown in Figure S8.

The channel \mathcal{E} that composes amplitude damping and dephasing is given by

$$\mathcal{E}_{\text{qk}}(t_{1\text{qb}}) : \rho_{\text{qk}} \mapsto \sum_{\substack{i=1,2 \\ j=1,2,3}} A_{i,\Gamma_1}(t_{1\text{qb}}) D_{j,\Gamma_{\phi}}(t_{1\text{qb}}) \rho_{\text{qk}} D_{j,\Gamma_{\phi}}^{\dagger}(t_{1\text{qb}}) A_{i,\Gamma_1}^{\dagger}(t_{1\text{qb}}), \quad (\text{S1})$$

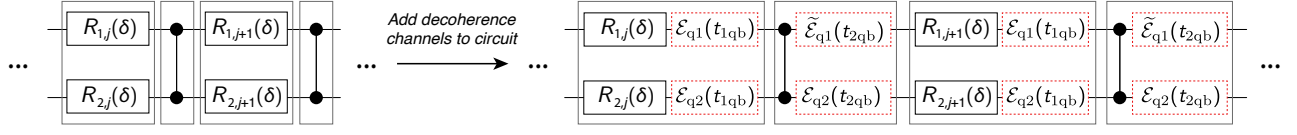


FIG. S8. Instrumenting the DME circuit for simulation of decoherence-induced errors.

where $A_{i,\Gamma_1}(t)$ is the amplitude damping process (with $\Gamma_1 = 1/T_1$), and $D_{j,\Gamma_\phi}(t)$ is the dephasing process ($\Gamma_\phi = 1/T_{2R} - 1/2T_1$), $\Gamma_{1,qk}$ and $\Gamma_{\phi,qk}$ are the appropriate coherence parameters for qubit k , and t is the time of the preceding single- or two-qubit gate on that qubit. The amplitude damping and dephasing Krauss operators are given by

$$A_{1,\Gamma_1}(t) = \begin{pmatrix} 1 & 0 \\ 0 & e^{-\Gamma_{1,qk}t/2} \end{pmatrix}, \quad A_{2,\Gamma_1}(t) = \begin{pmatrix} 0 & \sqrt{1 - e^{-\Gamma_{1,qk}t}} \\ 0 & 0 \end{pmatrix} \quad (S2)$$

$$D_{1,\Gamma_\phi}(t) = \begin{pmatrix} e^{-\Gamma_{\phi,qk}t/2} & 0 \\ 0 & e^{-\Gamma_{\phi,qk}t/2} \end{pmatrix}, \quad D_{2,\Gamma_\phi}(t) = \begin{pmatrix} \sqrt{1 - e^{-\Gamma_{\phi,qk}t}} & 0 \\ 0 & 0 \end{pmatrix}, \quad D_{3,\Gamma_\phi}(t) = \begin{pmatrix} 0 & 0 \\ 0 & \sqrt{1 - e^{-\Gamma_{\phi,qk}t}} \end{pmatrix}, \quad (S3)$$

The channel $\tilde{\mathcal{E}}$ is defined similarly to \mathcal{E} , but decoherence rates in the process definitions are replaced with their *effective* coherence parameters. The channel $\tilde{\mathcal{E}}$ thus accounts for the modified coherence properties as qubit 1 undergoes the CZ trajectory (see Figure S2).

Each instrumented circuit yields an SQM-dependent density matrix representing the simulated finite-coherence circuit output for that SQM realization. These density matrices are averaged over all 2^N SQM realizations (for a DME circuit with N steps), thus producing the ‘noisy’ simulated two-qubit DME output state, denoted ‘Sim. $F_s(\sigma_{\text{DME}}, \sigma_{\text{ideal}})$ with decoherence’ and plotted as a solid line in Figure 3B of the main text. For the simulation presented in the main paper we used parameters $T_1 = 20 \mu\text{s}$, $T_{2R} = 10 \mu\text{s}$ for both qubits, and effective coherence times for qubit 1 of $\tilde{T}_1 = 10 \mu\text{s}$ and $\tilde{T}_{2R} = 5 \mu\text{s}$ during the channel $\tilde{\mathcal{E}}$. These parameters are qualitatively consistent with, but overall reduced from, the measured parameters in Table S1. This difference may indicate additional coherent errors not captured by this model (e.g. from residual $\hat{\sigma}_Z \hat{\sigma}_Z$ -interaction or leakage out of the computational subspace).

-
- [S1] J. Koch, *et al.*, *Physical Review A* **76**, 042319 (2007).
[S2] M. D. Hutchings, *et al.*, *Phys. Rev. Applied* **8**, 044003 (2017).
[S3] R. Barends, *et al.*, *Phys. Rev. Lett.* **111**, 080502 (2013).
[S4] P. Klimov, *et al.*, *Phys. Rev. Lett.* **121**, 090502 (2018).
[S5] J. J. Burnett, *et al.*, *npj Quantum Inf* **5**, 1 (2019).
[S6] K. Jacobs, D. A. Steck, *Contemporary Physics* **47**, 279303 (2006).
[S7] W. M. Itano, D. J. Heinzen, J. Bollinger, D. Wineland, *Physical Review A* **41**, 2295 (1990).
[S8] M. A. Nielsen, I. L. Chuang, *Quantum Computation and Quantum Information: 10th Anniversary Edition* (Cambridge University Press, New York, NY, USA, 2011).
[S9] R. Barends, *et al.*, *Nature Communications* **6**, 7654 (2015).
[S10] J. Kelly, *et al.*, *Phys. Rev. Lett.* **112**, 240504 (2014).
[S11] J. M. Martinis, M. R. Geller, *Physical Review A* **90**, 022307 (2014).
[S12] M. Rol, *et al.*, *Phys. Rev. Lett.* **123**, 120502 (2019).
[S13] F. Vatan, C. Williams, *Phys. Rev. A* **69**, 032315 (2004).
[S14] Cirq-v0.5.0, <https://github.com/quantumlib/cirq>.
[S15] D. C. McKay, C. J. Wood, S. Sheldon, J. M. Chow, J. M. Gambetta, *Phys. Rev. A* **96**, 22330 (2017).
[S16] R. Barends, *et al.*, *Nature* **508**, 500 (2014).
[S17] Z. Chen, *Metrology of Quantum Control and Measurement in Superconducting Qubits*, Ph.D. thesis, University of California, Santa Barbara (2018).
[S18] J. Wallman, C. Granade, R. Harper, S. T. Flammia, *New J. Phys.* **17**, 113020 (2015).
[S19] T. Proctor, K. Rudinger, K. Young, M. Sarovar, R. Blume-Kohout, *Phys. Rev. Lett.* **119**, 130502 (2017).
[S20] J. J. Wallman, *Quantum* **2**, 47 (2018).
[S21] J. M. Chow, *et al.*, *Phys. Rev. A* **81** (2010).
[S22] K. Banaszek, G. M. D’Ariano, M. G. A. Paris, M. F. Sacchi, *Phys. Rev. A* **61**, 010304 (1999).
[S23] G. C. Knee, E. Bolduc, J. Leach, E. M. Gauger, *Phys. Rev. A* **98**, 062336 (2018).
[S24] B. Efron, *Ann. Statist.* **7**, 1 (1979).

[S25] W. K. Wootters, *Phys. Rev. Lett.* **80**, 2245 (1998).